# LETTER

# Glial–cell–derived neuroregulators control type 3 innate lymphoid cells and gut defence

Sales Ibiza[1]*, Bethania García-Cassani[1]*, Hélder Ribeiro[1], Tânia Carvalho[1], Luís Almeida[1], Rute Marques[2]†, Ana M. Misic[3]†, Casey Bartow-McKenney[3], Denise M. Larson[4], William J. Pavan[4], Gérard Eberl[2], Elizabeth A. Grice[3] & Henrique Veiga-Fernandes[1,5]

**Group 3 innate lymphoid cells (ILC3) are major regulators of inflammation and infection at mucosal barriers[1]. ILC3 development is thought to be programmed[1], but how ILC3 perceive, integrate and respond to local environmental signals remains unclear. Here we show that ILC3 in mice sense their environment and control gut defence as part of a glial–ILC3–epithelial cell unit orchestrated by neurotrophic factors. We found that enteric ILC3 express the neuroregulatory receptor RET. ILC3-autonomous *Ret* ablation led to decreased innate interleukin-22 (IL-22), impaired epithelial reactivity, dysbiosis and increased susceptibility to bowel inflammation and infection. Neurotrophic factors directly controlled innate *Il22* downstream of the p38 MAPK/ERK-AKT cascade and STAT3 activation. Notably, ILC3 were adjacent to neurotrophic-factor-expressing glial cells that exhibited stellate-shaped projections into ILC3 aggregates. Glial cells sensed microenvironmental cues in a MYD88-dependent manner to control neurotrophic factors and innate IL-22. Accordingly, glial-intrinsic *Myd88* deletion led to impaired production of ILC3-derived IL-22 and a pronounced propensity towards gut inflammation and infection. Our work sheds light on a novel multi-tissue defence unit, revealing that glial cells are central hubs of neuron and innate immune regulation by neurotrophic factor signals.**

ILC3 produce proinflammatory cytokines, and regulate mucosal homeostasis and anti-microbial defence[1]. In addition to their well-established developmentally regulated program, ILC3 are also controlled by microbial and dietary signals[1–6], suggesting that ILC3 possess other unexpected environment-sensing strategies. Neurotrophic factors are extracellular environmental cues to neurons and include the glial-derived neurotrophic factor (GDNF) family ligands (GFL) that activate the tyrosine kinase receptor RET in the nervous system, kidney and haematopoietic progenitors[7–11].

Analysis of gut lamina propria revealed that ILC3 express high levels of *Ret*[7,12] (Fig.1a), a finding confirmed at the protein level and by reporter *Ret*[GFP] knock-in mice[13] (Fig. 1b–d and Extended Data Fig. 1a–d). ILC3 subsets expressed *Ret*[GFP] and aggregated in cryptopatches and isolated lymphoid follicles (ILF), suggesting a role of neuroregulators in ILC3 (Fig.1b–d and Extended Data Fig. 1b–j). To explore this hypothesis, we transplanted fetal liver cells from *Ret* competent (*Ret*[WT/GFP]) or deficient (*Ret*[GFP/GFP])[13] animals into alymphoid *Rag1*^{−/−}γc^{−/−} hosts. *Ret*-deficient chimaeras revealed unperturbed ILC3 and cryptopatch development (Fig. 1e). Notably, IL-22-expressing ILC3 were largely reduced despite normal IL-22 production by T cells (Fig.1f, g). In contrast, innate IL-17 was unaffected by *Ret* ablation (Fig.1f and Extended Data Fig. 2a). In agreement with this, analysis of gain-of-function *Ret*[MEN2B] mice[14] revealed a selective
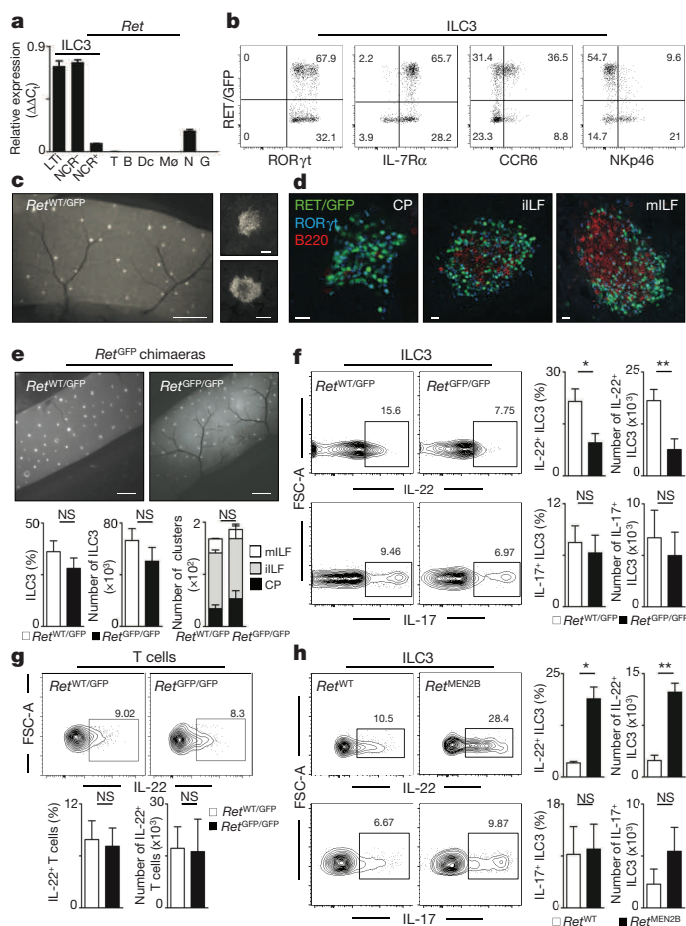


**Figure 1 | The neurotrophic factor receptor RET drives enteric ILC3-derived IL-22. a**, Relative expression of *Ret* in lymphoid tissue initiator cells (LTi), natural cytotoxicity receptor (NCR)⁻ and NCR⁺ ILC3 subsets, T cells (T), B cells (B), dendritic cells (Dc), macrophages (Mø), enteric neurons (N) and mucosal glial cells (G). **b**, *Ret*[GFP] ILC3 subsets in the gut. **c**, Left, *Ret*[GFP] gut. Right, ILC3 aggregates. White, GFP. **d**, Enteric cryptopatches (CP), immature (iILF) and mature (mILF) isolated lymphoid follicles. Green, RET/GFP; blue, RORγt; red, B220. **e**, Small intestine of *Ret*[GFP] chimaeras (*n* = 15). **f, g**, Enteric ILC3 and T cells from *Ret*[GFP] chimaeras. *Ret*[WT/GFP], *n* = 25; *Ret*[GFP/GFP], *n* = 22. **h**, Enteric ILC3 from *Ret*[MEN2B] mice (*n* = 7). Scale bars, 1 mm (**c** left, **e**); 50 μm (**c** right); 30 μm (**d**). Data are representative of 4 independent experiments. Error bars show s.e.m. *P < 0.05, **P < 0.01; NS, not significant.

[1]Instituto de Medicina Molecular, Faculdade de Medicina de Lisboa, Av. Prof. Egas Moniz, Edifício Egas Moniz, 1649-028 Lisboa, Portugal. [2]Microenvironment and Immunity Unit, Institut Pasteur, 25 Rue du Docteur Roux, 75724 Paris, France. [3]Department of Dermatology, Perelman School of Medicine, University of Pennsylvania, 421 Curie Blvd, 1007 Biomedical Research Building, Philadelphia, Pennsylvania 19104, USA. [4]Genetic Disease Research Branch, National Human Genome Research Institute, National Institutes of Health, Bethesda, Maryland 20892, USA. [5]Champalimaud Research, Champalimaud Centre for the Unknown, 1400-038 Lisboa, Portugal. †Present addresses: INSERM, U1163, Laboratory of Intestinal Immunity, and Université Paris Descartes-Sorbonne Paris Cité and Institut Imagine, Paris, France (R.M.); Center for Host-Microbial Interactions, Department of Pathobiology, School of Veterinary Medicine, University of Pennsylvania, Philadelphia, Pensylvania 19104, USA (A.M.M.).
*These authors contributed equally to this work.

increase of IL-22-producing ILC3, whereas their IL-17-producing counterparts were unaffected (Fig.1h and Extended Data Fig. 2b). To more specifically evaluate the effects of RET in ILC3, we deleted *Ret* in ROR$\gamma$t-expressing cells by breeding *Rorgt*-Cre with *Ret*^{fl/fl} mice[15,16] (Extended Data Fig. 3a, b). Analysis of *Rorgt*-Cre*Ret*^{fl/fl} (*Ret*$^\Delta$) mice revealed selective and extensive reduction of ILC3-derived IL-22, but normal IL-22-producing T cells (Fig. 2a and Extended Data Fig. 3c, d). IL-22 acts on epithelial cells to induce reactivity and repair genes[1]. When compared to their wild-type littermate controls, the *Ret*$^\Delta$ epithelium revealed normal morphology, proliferation and paracellular permeability, but a marked reduction of epithelial reactivity and repair genes (Fig. 2b and Extended Data Fig. 3e–h). Accordingly, the *Ret*[MEN2B] epithelium displayed increased levels of these molecules in an IL-22-dependent manner (Fig. 2b and Extended Data Fig. 3i). These results indicate that RET signals selectively control innate IL-22 and shape intestinal epithelial reactivity.

To determine whether neurotrophic factors regulate intestinal defence, we tested how varying degrees of RET signals control enteric aggressions. Whereas *Ret*$^\Delta$ mice treated with dextran sodium sulfate (DSS) had increased weight loss and inflammation, reduced IL-22-producing ILC3, decreased epithelial reactivity/repair genes and pronounced bacterial translocation from the gut, *Ret*[MEN2B] mutants were highly protected compared to their wild-type littermate controls

(Fig. 2c–j and Extended Data Fig. 4). As DSS largely causes epithelial injury, we tested whether ILC3-autonomous RET signals are required to control infection. To this end, *Ret*$^\Delta$ mice were bred with *Rag1*$^{-/-}$ mice to formally exclude adaptive T-cell effects. The resulting *Rag1*$^{-/-}$*Ret*$^\Delta$ mice were infected with the attaching and effacing bacteria *Citrobacter rodentium*. When compared to their littermate controls, *Rag1*$^{-/-}$*Ret*$^\Delta$ mice had marked gut inflammation, reduced IL-22-producing ILC3, increased *C. rodentium* infection and translocation, reduced epithelial reactivity genes, increased weight loss and reduced survival (Fig. 2k–n and Extended Data Fig. 5). Altogether, these data indicate that ILC3-intrinsic neurotrophic factor cues regulate gut defence and homeostasis.

We used a multi-tissue organoid system to show that IL-22 is the molecular link between RET-dependent ILC3 activation and epithelial reactivity. Addition of GFL to ILC3–epithelial organoids strongly induced epithelial reactivity genes in an IL-22- and RET-dependent manner (Fig. 3a, b and Extended Data Fig. 6a). To further examine how RET signals control innate IL-22, we investigated a gene signature
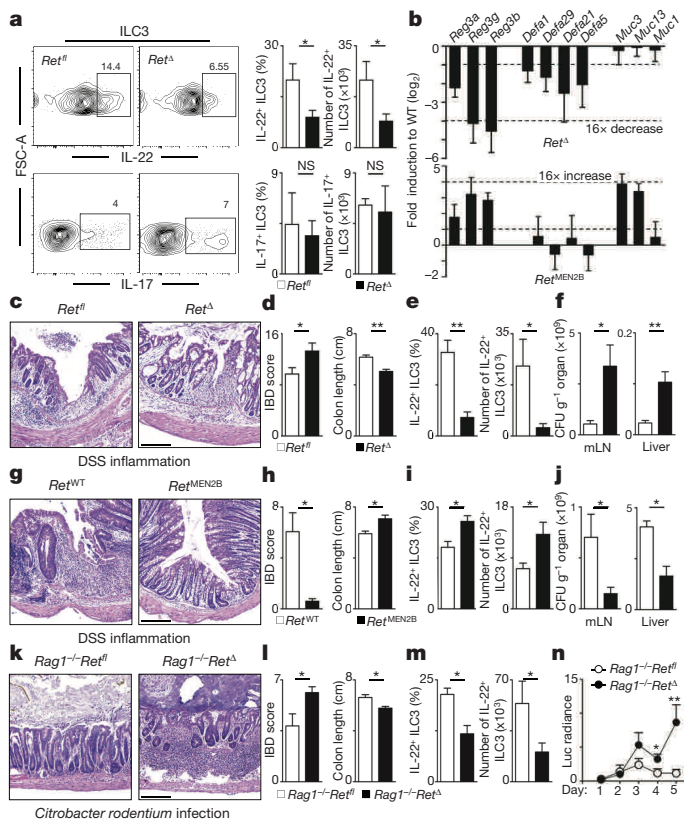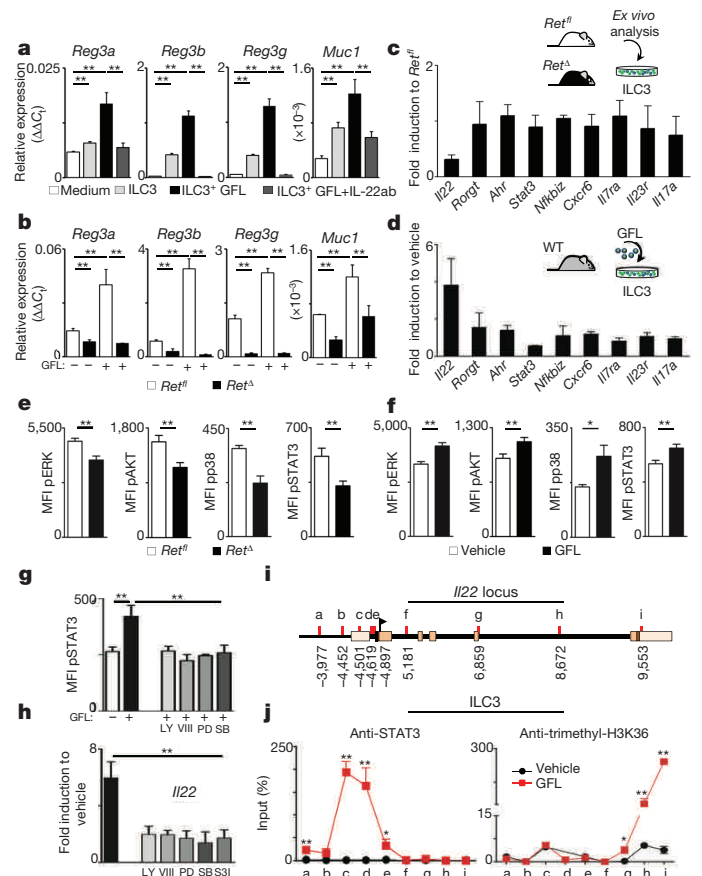


**Figure 2 | ILC3-intrinsic RET signals regulate gut defence. a**, ILC3-derived cytokines (*n* = 11). **b**, Gene expression in the epithelium of *Ret*$^\Delta$ and *Ret*[MEN2B] mice compared to their wild-type littermate controls (*n* = 7). **c–f**, DSS treatment in *Ret*[fl] and *Ret*$^\Delta$ mice (*n* = 8). **c**, Histopathology. **d**, Inflammation score and colon length. **e**, Innate IL-22. **f**, Bacterial translocation. CFU, colony-forming unit. **g–j**, DSS treatment in *Ret*[WT] and *Ret*[MEN2B] mice (*n* = 8). **g**, Histopathology. **h**, Inflammation score and colon length. **i**, Innate IL-22. **j**, Bacterial translocation. mLN, mesenteric lymph node. **k–n**, *C. rodentium* infection in *Rag1*$^{-/-}$*Ret*[fl] (*n* = 15) and *Rag1*$^{-/-}$*Ret*$^\Delta$ (*n* = 17) mice. **k**, Histopathology. **l**, Inflammation score and colon length. **m**, Innate IL-22. **n**, Infection burden. Scale bars, 200 μm. Data are representative of 4 independent experiments. Error bars show s.e.m. *$P < 0.05$, **$P < 0.01$.



**Figure 3 | ILC3-autonomous RET signals directly control *Il22* downstream of pSTAT3. a, b**, Epithelial-ILC3 organoids (*n* = 9). **c**, Gene expression in *Ret*$^\Delta$ ILC3 compared to their wild-type controls (*n* = 4). **d**, Gene expression in ILC3 after activation by GFL (*n* = 4). **e**, Enteric *Ret*$^\Delta$ ILC3. pERK, *n* = 8; pAKT, *n* = 12; phosphorylated p38/MAP kinase, *n* = 6; pSTAT3, *n* = 14. MFI, mean fluorescence intensity. **f**, Enteric ILC3 activation by GFL. pERK, *n* = 10; pAKT, *n* = 16; phosphorylated p38/MAP kinase, *n* = 3; pSTAT3, *n* = 15. **g**, pSTAT3 expression in enteric ILC3 cultured with medium (*n* = 7), GFL (*n* = 11) or GFL and inhibitors for: p38 MAPK/ERK-AKT (LY) (*n* = 7); ERK (PD) (*n* = 7); AKT (VIII) (*n* = 8); and p38 MAPK (SB) (*n* = 6). **h**, *Il22* in enteric ILC3 cultured with GFL (*n* = 17) or GFL and the inhibitors LY (*n* = 18); PD (*n* = 16); VIII (*n* = 15); SB (*n* = 15); and the STAT3 inhibitor (S3I) (*n* = 8). **i**, *Il22* locus. The letters a–i in this panel indicate putative STAT3 binding sites and primer location (see Methods). **j**, ChIP analysis of ILC3 stimulated with GFL (*n* = 10). Data are representative of 3 independent experiments. Error bars show s.e.m. *$P < 0.05$, **$P < 0.01$.

associated with ILC identity[1]. Whereas the master ILC transcription factors *Runx1*, *Id2*, *Gata3*, *Rora, Rorgt, Ahr* and *Stat3* were unperturbed, *Il22* was significantly reduced in *Ret*[Δ] ILC3 (Fig. 3c and Extended Data Fig. 6b). Accordingly, activation of ILC3 with all or distinct GFL–GFRα pairs *in trans* efficiently increased *Il22* despite normal expression of other ILC3-related genes (Fig. 3d and Extended Data Fig. 6c). Activation of RET by GFL leads to p38 MAPK/ERK-AKT cascade activation in neurons, whereas phosphorylation of STAT3 shapes *Il22* expression[7,17]. Analysis of *Ret*[Δ] ILC3 revealed hypo-phosphorylated ERK1/2, AKT, p38/MAP kinase and STAT3 (Fig. 3e and Extended Data Fig. 6d). Accordingly, GFL-induced RET activation in ILC3 led to rapid ERK1/2, AKT, p38/MAP kinase and STAT3 phosphorylation and increased *Il22* transcription (Fig. 3d, f and Extended Data Fig. 6e, f). Accordingly, inhibition of ERK, AKT or p38/MAP kinase upon GFL activation led to impaired STAT3 activation and *Il22* expression (Fig. 3g, h). Finally, inhibition of STAT3 upon GFL-induced RET activation led to decreased *Il22* (Fig. 3h). To examine whether GFL directly regulate *Il22*, we performed chromatin immunoprecipitation (ChIP)[18] (Fig. 3i, j). Stimulation of ILC3 with GFL resulted in increased binding of pSTAT3 in the *Il22* promoter and increased trimethyl-H3K36 at the 3′ end of *Il22,* indicating active *Il22*-transcribed regions[19] (Fig. 3d, j). Thus, cell-autonomous RET signals control ILC3 function and gut defence by direct regulation of *Il22* downstream of STAT3 activation.

Propensity towards inflammation and dysregulation of intestinal homeostasis have been associated with dysbiosis[20,21]. When compared to their wild-type littermates, *Ret*[Δ] mice have altered microbial communities as evidenced by quantitative analysis, weighted UniFrac analysis and significantly altered levels of *Sutterella*, unclassified *Clostridiales* and *Bacteroides* (Fig. 4a and Extended Data Fig. 7). Discrete microbial communities may have transmissible colitogenic potential[20,21]. Nevertheless, germ-free mice colonized with the microbiota of *Ret*[Δ] or their control littermates revealed similar susceptibility to DSS-induced colitis and identical innate IL-22 production (Fig. 4b–d). In agreement, co-housed *Ret*[Δ] and wild-type littermates had different propensity towards intestinal inflammation (Fig. 2c, d). Together, these data indicate that dysbiosis *per se* is insufficient to cause altered innate IL-22 and susceptibility to gut inflammation as observed in *Ret*[Δ] mice (Fig. 2c–f). Thus, we hypothesised that GFL-producing cells integrate commensal and environmental signals to control innate IL-22. Accordingly, antibiotic treatment of *Ret*[Δ] and their wild-type littermate controls resulted in similar ILC3-derived IL-22 (ref. 22) (Fig. 4e).

Neurotrophic factors of the GDNF family were shown to be produced by enteric glial cells, which are neuron-satellites expressing the glial fibrillary acidic protein (GFAP)[7,23]. Notably, double reporter mice for ILC3 (*Ret*[GFP]) and glial cells (*Gfap*-Cre*Rosa26*[RFP]) revealed that stellate-shaped projections of glial cells are adjacent (4.35 ± 1.42 μm) to RORγt[+] ILC3 within cryptopatches (Fig. 4f and Extended Data Fig. 8a). These data suggest the existence of paracrine glial–ILC3 cross-talk orchestrated by neurotrophic factors. Accordingly, lamina propria glial cells were the main producers of GFL (Extended Data Fig. 8b). Recent studies have shown that glial cells express pattern recognition receptors, notably Toll-like receptors (TLRs)[24,25]. Activation of neurosphere-derived glial cells revealed they specifically respond to TLR2, TLR4, and the alarmins IL-1β and IL-33, which efficiently controlled GFL expression and induced robust innate *Il22* in a MYD88-dependent manner (Fig. 4g–i and Extended Data Fig. 8c–g). To formally demonstrate the physiological importance of MYD88-dependent glial cell sensing on innate IL-22 production, we deleted *Myd88* in GFAP-expressing glial cells by breeding *Gfap*-Cre with *Myd88*^{fl/fl} mice[26,27]. Remarkably, glial-intrinsic deletion of *Myd88* resulted in decreased intestinal GFL, increased gut inflammation, impaired ILC3-derived IL-22, and increased weight loss (Fig. 4j–m; Extended Data Fig. 9a–d). In agreement, *Gfap*-Cre*Myd88*[Δ] mice had increased susceptible to *C. rodentium* infection (Extended Data Fig. 9e–h). Thus, mucosal glial cells orchestrate innate IL-22 via neurotrophic factors,
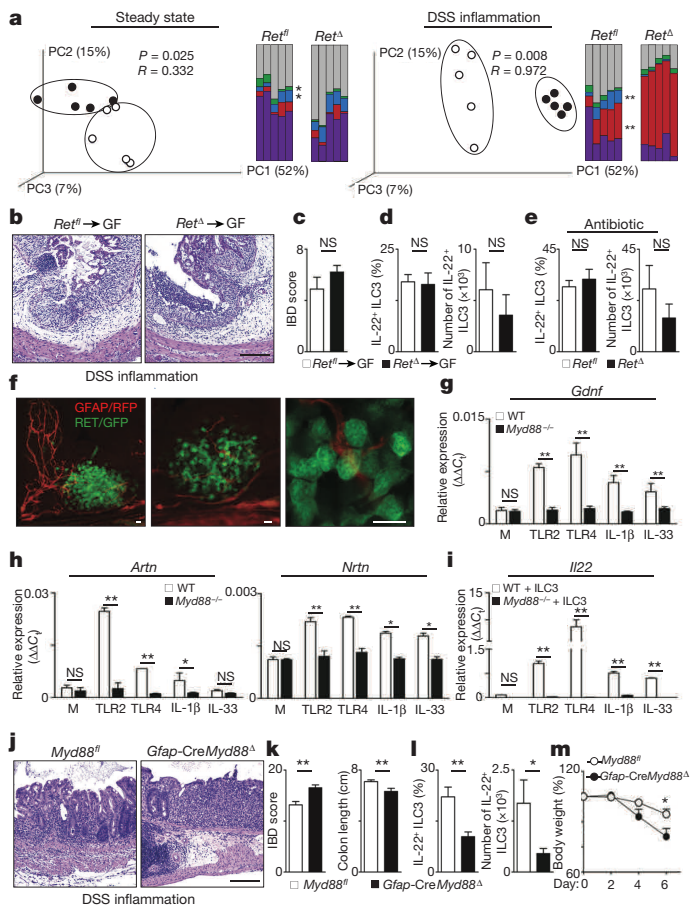


**Figure 4 | Glial cells set GFL expression and innate IL-22 via MYD88-dependent sensing of the microenvironment. a,** Weighted Unifrac PCoA analysis and genus-level comparisons from co-housed *Ret*[fl] (white circles) and *Ret*[Δ] (black circles) littermates (*n* = 5). Purple, unclassified *S24-7*; red, *Bacteroides*; green, *Sutterella*; blue, unclassified *Clostridiales*; grey, other. **b–d,** DSS treatment of germ-free (GF) mice (*n* = 5) colonized with microbiota from *Ret*[fl] or *Ret*[Δ] mice. **b,** Histopathology. **c,** Inflammation score. **d,** Innate IL-22. **e,** Innate IL-22 after antibiotic treatment (*n* = 8). **f,** *Ret*[GFP]*Gfap*-Cre*Rosa26*[RFP] mice. Green, RET/GFP; red, GFAP/RFP. **g, h,** Glial cell activation with TLR2, TLR4, IL-1β receptor and IL-33 receptor ligands (*n* = 6). **i,** TLR ligands, IL-1β and IL-33 activation of co-cultured ILC3 with wild-type (white bars) or *Myd88*^{−/−} glial cells (black bars) (*n* = 6). **j–m,** DSS treatment of *Gfap*-Cre*Myd88*[Δ] mice (*n* = 12). **j,** Histopathology. **k,** Inflammation score and colon length. **l,** Innate IL-22. **m,** Body weight. Scale bars, 200 μm (**b, j**); 10 μm (**f**). Data are representative of 3–4 independent experiments. Error bars show s.e.m. **P* < 0.05, ***P* < 0.01.

downstream of MYD88-dependent sensing of commensal products and alarmins.

Defining the mechanisms by which ILC3 integrate environmental cues is critical to understanding mucosal homeostasis. Our work sheds light on the relationships between ILC3 and their microenvironment, notably through decoding a novel glial–ILC3–epithelial cell unit orchestrated by neurotrophic factors (Extended Data Fig. 10). Glial-derived neurotrophic factors operate in an ILC3-intrinsic manner by activating the tyrosine kinase RET, which directly regulates innate IL-22 downstream of p38 MAPK/ERK-AKT and STAT3 phosphorylation (Extended Data Fig. 10). Future studies will further elucidate the mechanisms inducing RET expression in ILC3.

Our data demonstrate that, in addition to their well-established capacity to integrate dendritic-cell-derived cytokines[1], ILC3 perceive distinct multi-tissue regulatory signals leading to STAT3 activity and IL-22 expression, notably by integration of glial-cell-derived neuroregulators. Thus, rather than providing hard-wired signals for

ILC3-immunity, we propose that RET signalling induces fine-tuned innate IL-22 production that leads to efficient gut homeostasis and defence.

Previous studies demonstrated that neurons may indirectly shape fetal lymphoid tissue inducer cell aggregation via regulation of mesenchymal cells and that ablation of glial cells leads to gut inflammation[28,29]; here we reveal that glial cells are central hubs of neuronal and innate immune regulation. Notably, neurotrophic factors are the molecular link between glial cell sensing, innate IL-22 and intestinal epithelial defence. Thus, it is tempting to speculate that glial–immune cell units might be also critical to the homeostasis of other barriers, notably in the skin, lung and brain[30]. From an evolutionary perspective, coordination of innate immunity and neuronal function may ensure efficient mucosal homeostasis and a co-regulated neuro-immune response to various environmental challenges, including xenobiotics, intestinal infection, dietary aggressions and cancer.

**Online Content** Methods, along with any additional Extended Data display items and Source Data, are available in the online version of the paper; references unique to these sections appear only in the online paper.

1. Artis, D. & Spits, H. The biology of innate lymphoid cells. *Nature* **517,** 293–301 (2015).
2. van de Pavert, S. A. *et al.* Maternal retinoids control type 3 innate lymphoid cells and set the offspring immunity. *Nature* **508,** 123–127 (2014).
3. Spencer, S. P. *et al.* Adaptation of innate lymphoid cells to a micronutrient deficiency promotes type 2 barrier immunity. *Science* **343,** 432–437 (2014).
4. Kiss, E. A. *et al.* Natural aryl hydrocarbon receptor ligands control organogenesis of intestinal lymphoid follicles. *Science* **334,** 1561–1565 (2011).
5. Lee, J. S. *et al.* AHR drives the development of gut ILC22 cells and postnatal lymphoid tissues via pathways dependent on and independent of Notch. *Nat. Immunol.* **13,** 144–151 (2011).
6. Qiu, J. *et al.* The aryl hydrocarbon receptor regulates gut immunity through modulation of innate lymphoid cells. *Immunity* **36,** 92–104 (2012).
7. Mulligan, L. M. RET revisited: expanding the oncogenic portfolio. *Nat. Rev. Cancer* **14,** 173–186 (2014).
8. Fonseca-Pereira, D. *et al.* The neurotrophic factor receptor RET drives haematopoietic stem cell survival and function. *Nature* **514,** 98–101 (2014).
9. Veiga-Fernandes, H. *et al.* Tyrosine kinase receptor RET is a key regulator of Peyer's patch organogenesis. *Nature* **446,** 547–551 (2007).
10. Patel, A. *et al.* Differential RET signaling pathways drive development of the enteric lymphoid and nervous systems. *Sci. Signal.* **5,** ra55 (2012).
11. Almeida, A. R. *et al.* The neurotrophic factor receptor RET regulates IL-10 production by in vitro polarised T helper 2 cells. *Eur. J. Immunol.* **44,** 3605–3613 (2014).
12. Robinette, M. L. *et al.* Transcriptional programs define molecular characteristics of innate lymphoid cell classes and subsets. *Nat. Immunol.* **16,** 306–317 (2015).
13. Hoshi, M., Batourina, E., Mendelsohn, C. & Jain, S. Novel mechanisms of early upper and lower urinary tract patterning regulated by RetY1015 docking tyrosine in mice. *Development* **139,** 2405–2415 (2012).
14. Smith-Hicks, C. L., Sizer, K. C., Powers, J. F., Tischler, A. S. & Costantini, F. C-cell hyperplasia, pheochromocytoma and sympathoadrenal malformation in a mouse model of multiple endocrine neoplasia type 2B. *EMBO J.* **19,** 612–622 (2000).
15. Sawa, S. *et al.* Lineage relationship analysis of RORγt+ innate lymphoid cells. *Science* **330,** 665–669 (2010).
16. Almeida, A. R. *et al.* RET/GFRα signals are dispensable for thymic T cell development *in vivo*. *PLoS One* **7,** e52949 (2012).
17. Rutz, S., Wang, X. & Ouyang, W. The IL-20 subfamily of cytokines--from host defence to tissue homeostasis. *Nat. Rev. Immunol.* **14,** 783–795 (2014).
18. Xu, W. *et al.* NFIL3 orchestrates the emergence of common helper innate lymphoid cell precursors. *Cell Reports* **10,** 2043–2054 (2015).
19. Wen, H. *et al.* ZMYND11 links histone H3.3K36me3 to transcription elongation and tumour suppression. *Nature* **508,** 263–268 (2014).
20. Garrett, W. S. *et al. Enterobacteriaceae* act in concert with the gut microbiota to induce spontaneous and maternally transmitted colitis. *Cell Host Microbe* **8,** 292–300 (2010).
21. Elinav, E. *et al.* NLRP6 inflammasome regulates colonic microbial ecology and risk for colitis. *Cell* **145,** 745–757 (2011).
22. Rakoff-Nahoum, S., Paglino, J., Eslami-Varzaneh, F., Edberg, S. & Medzhitov, R. Recognition of commensal microflora by toll-like receptors is required for intestinal homeostasis. *Cell* **118,** 229–241 (2004).
23. Neunlist, M. *et al.* The digestive neuronal-glial-epithelial unit: a new actor in gut health and disease. *Nat. Rev. Gastroenterol. Hepatol.* **10,** 90–100 (2013).
24. Brun, P. *et al.* Toll-like receptor 2 regulates intestinal inflammation by controlling integrity of the enteric nervous system. *Gastroenterology* **145,** 1323–1333 (2013).
25. Kabouridis, P. S. *et al.* Microbiota controls the homeostasis of glial cells in the gut lamina propria. *Neuron* **85,** 289–295 (2015).
26. Zhuo, L. *et al.* hGFAP-cre transgenic mice for manipulation of glial and neuronal function in vivo. *Genesis* **31,** 85–94 (2001).
27. Hou, B., Reizis, B. & DeFranco, A. L. Toll-like receptors activate innate and adaptive immunity by using dendritic cell-intrinsic and -extrinsic mechanisms. *Immunity* **29,** 272–282 (2008).
28. van de Pavert, S. A. *et al.* Chemokine CXCL13 is essential for lymph node initiation and is induced by retinoic acid and neuronal stimulation. *Nat. Immunol.* **10,** 1193–1199 (2009).
29. Bush, T. G. *et al.* Fulminant jejuno-ileitis following ablation of enteric glia in adult transgenic mice. *Cell* **93,** 189–201 (1998).
30. Veiga-Fernandes, H. & Mucida, D. Neuro-Immune Interactions at Barrier Surfaces. *Cell* **165,** 801–811 (2016).

**Author Contributions** S.I. and B.G.-C. designed, performed and analysed the experiments in Figs 1–4 and Extended Data Figs 1–9. T.C. analysed the experiments in Figs 2c, d, g, h, k, l, 4j, k, and Extended Data Figs 3e and 4e. H.R. performed and analysed the experiments in Figs 2f, j, n, 4a, m, Extended Data Figs 5a–c, e–j, 7a and 9f–h. L.A. contributed to experiments in Fig. 3a, b and Extended Data Fig. 6a. D.M.L., W.J.P., A.M.M., C.B.M. and E.A.G. performed and analysed the experiments in Fig. 4a and Extended Data Fig. 7b, c. R.M. and G.E. designed, performed and analysed the experiments in Fig. 4b–d. H.V.-F. supervised the work, planned the experiments and wrote the manuscript.

## METHODS

**Data reporting.** The experiments were not randomized. The investigators were not blinded to allocation during experiments and outcome assessment, unless stated otherwise. Power analysis was used to estimate sample size.

**Mice.** C57BL/6J mice were purchased from Charles River. $Ret^{GFP}$ (ref. 13), $Rag1^{-/-}\gamma c^{-/-}$ (refs 31, 32), $Ret^{MEN2B}$ (ref. 14), $Rosa26^{YFP}$ (ref. 33), $Rosa26^{RFP}$ (ref. 34), $Ret^{fl/fl}$ (ref. 16), $Rorgt$-Cre[15], $Il1b^{-/-}$ (ref. 35) and $Myd88^{-/-}$ (ref. 36) were in a full C57BL/6J background. $Gfap$-Cre[26] bred to $Myd88^{fl/fl}$ (ref. 27) were in F8–F9 to a C57Bl/6J background. All lines were bred and maintained at IMM Lisboa animal facility. Mice were systematically compared with co-housed littermate controls. Both males and females were used in this study. Randomization and blinding were not used unless stated otherwise. All animal experiments were approved by national and institutional ethical committees, respectively, Direção Geral de Veterinária and iMM Lisboa ethical committee. Germ-free mice were housed at Instituto Gulbenkian de Ciência, Portugal, and Institut Pasteur, France, in accordance to institutional guidelines for animal care. Power analysis was performed to estimate the number of experimental mice.

**Generation of fetal liver chimeras.** For reconstitution experiments, $5 \times 10^6$ fetal liver cells were isolated from E14.5 $Ret^{WT/GFP}$ or $Ret^{GFP/GFP}$ mice and injected intravenously into non-lethally irradiated (200 rad) alymphoid $Rag1^{-/-}\gamma c^{-/-}$ hosts. Mice were analysed 8 weeks after transplantation.

**DSS-induced colitis.** Dextran sodium sulfate (DSS) (molecular mass 36,000–50,000 Da; MP Biomedicals) was added into drinking water 3% (w/v) for 5 days followed by 2 days of regular water. Mice were analysed at day 7. Body weight, presence of blood and stool consistency was assessed daily.

***Citrobacter rodentium* infection.** Infection with *Citrobacter rodentium* ICC180 (derived from DBS100 strain)[37] was performed by gavage inoculation of $10^9$ colony-forming units[37,38]. Acquisition and quantification of luciferase signal was performed in an IVIS system (Caliper Life Sciences). Throughout infection, weight loss, diarrhoea and bloody stools were monitored daily.

**Antibiotic treatment.** Pregnant females or newborn mice were treated with streptomycin $5\,g\,l^{-1}$, ampicillin $1\,g\,l^{-1}$ and colistin $1\,g\,l^{-1}$ (Sigma-Aldrich) into drinking water with 3% sucrose. Control mice were given 3% sucrose in drinking water as previously described[22].

**Microscopy.** Intestines from $Ret^{GFP}$ and $Ret^{GFP}$ chimaeras were imaged in a Zeiss Lumar V12 fluorescence stereo microscope with a NeoLumar S $0.8\times$ objective using the GFP filter. Whole-mount analysis was performed as previously described[2,9]. Briefly, adult intestines were flushed with cold PBS (Gibco) and opened longitudinally. Mucus and epithelium was removed and intestines were fixed in 4% PFA (Sigma-Aldrich) at room temperature for 10 mins and incubated in blocking/permeabilizing buffer solution (PBS containing 2% BSA, 2% goat serum, 0.6% Triton X-100). To visualise three-dimensional structures of the small intestine, samples were cleared with benzyl alcohol-benzyl benzoate (Sigma-Aldrich) before dehydration in methanol[2,9]. For analysis of thick gut sections, intestines were fixed with 4% PFA at 4 °C overnight and were then included in 4% low-melting temperature agarose (Invitrogen). Sections of $100\,\mu m$ were obtained with a Leica VT1200/VT1200 S vibratome and embedded in Mowiol (Calbiochem)[2]. Slides or whole-mount samples were incubated overnight or for 1–2 days respectively at 4 °C using the following antibodies: rat monoclonal anti-B220 (RA3-6B2) (eBioscience), mouse monoclonal anti-RORγt (Q31-378) (BD Pharmigen), mouse monoclonal anti-GFAP (GA-5) (Sigma-Aldrich), mouse monoclonal anti-GFAP Cy3 (GA-5) (Abcam), anti-GDNF antibody (Abcam), DAPI (4′,6-Diamidino-2-Phenylindole, Dihydrochloride) (Invitrogen). A647 goat anti-rat, A568 goat anti-rat, A647 goat anti-mouse, A488 rabbit anti-GFP, and A488 goat anti-rabbit secondary antibodies were purchased from Invitrogen. Neurospheres and cultured glial cells were fixed in PFA 4% for 10 minutes at room temperature and permeabilized in PBS-Triton 0.1% within 30 seconds. After several washing steps with PBS, cells were incubated with antibodies for 3 h at room temperature and then mounted in Mowiol[39]. Samples were acquired on a Zeiss LSM710 confocal microscope using EC Plan-Neofluar $10\times/0.30$ M27, Plan Apochromat $20\times/0.8$ M27 and EC Plan-Neofluar $40\times/1.30$ objectives. Three-dimensional reconstruction of images was achieved using Imaris software and snapshot pictures were obtained from the three-dimensional images. For analysis of confocal images, cells were counted using in-house software, written in MATLAB (Mathworks, Natick, MA). Briefly, single-cell ILC3 nuclei were identified by RORγt by thresholding and particle analysis. Regions of interest (ROIs) (Extended Data Fig.1i; bottom panels) were defined from each nucleus for analysis in the GFP channel, where staining was considered positive if a minimum number of pixels (usually 20) were above a given threshold. The software allows for batch processing of multiple images and generates individual report images for user verification of cell-counting results and co-expression analysis (https://imm.medicina.ulisboa.pt/en/servicos-e-recursos/technical-facilities/bioimaging).

**Histopathology analysis.** Colon samples were fixed in 10% neutral buffered formalin. The colon was prepared in multiple cross-sections or 'swiss roll' technique[40],

routine-processed for paraffin embedding and 3–4 μm sections were stained with haematoxylin and eosin. Enteric lesions were scored by a pathologist blinded to experimental groups, according to previously published criteria[41–43]. Briefly, lesions were individually scored (0–4 increasing severity) for the following criteria: 1, mucosal loss; 2, mucosal epithelial hyperplasia; 3, degree of inflammation; 4, extent of the section affected in any manner; and 5, extent of the section affected in the most severe manner as previously described[43]. Final scores were derived by summing the individual lesion and the extent scores. The internal diameter of the crypts was measured in at least five fields ($10\times$ magnification), corresponding to the hotspots in which the most severe changes in crypt architecture were seen. Measurements were performed in an average of 35 crypts per mouse, from proximal to distal colon. Intestinal villus height was measured in the jejunum. Measurements were performed in slides scanned using a Hamamatsu Nanozoomer SQ digital slide scanner running NDP Scan software.

**Enteric glial cell isolation.** Enteric glial cells isolation was adapted from previously described protocols[44,45]. Briefly, the muscularis layer was separated from the submucosa with surgical forceps under a dissection microscope (SteREO Lumar. V12, Zeiss). The lamina propria was scraped mechanically from the underlying submucosa using 1.5-mm cover-slips (Thermo Scientific). Isolated tissues were collected and digested with Liberase TM ($7,5\,\mu g\,ml^{-1}$; Roche) and DNase I ($0.1\,mg\,ml^{-1}$; Roche) in RPMI supplemented with 1% HEPES, sodium pyruvate, glutamine, streptomycin and penicillin and 0.1% β-mercaptoethanol (Gibco) for approximately 40 min at 37 °C. Single-cell suspensions were passed through a 100-μm cell strainer (BD Biosciences) to eliminate clumps and debris.

**Flow cytometry and cell sorting.** Lamina propria cells were isolated as previously described[46]. Briefly, intestines were digested with collagenase D ($0.5\,mg\,ml^{-1}$; Roche) and DNase I ($0.1\,mg\,ml^{-1}$; Roche) in RPMI supplemented with 10% FBS, 1% HEPES, sodium pyruvate, glutamine, streptomycin and penicillin and 0.1% β-mercaptoethanol (Gibco) for approximately 30 min at 37 °C under gentle agitation. For cytokine analysis, cell suspensions were incubated 4 h in PMA/ionomycin (Sigma-Aldrich) and brefeldin A (eBioscience) at 37 °C. Intracellular staining was performed using IC fixation/permeabilization kit (eBioscience). Cells were stained using PBS, 1% FBS, 1% HEPES and 0.6% EDTA (Gibco). Flow cytometry analysis and cell sorting was performed using FORTESSA and FACSAria flow cytometers (BD Biosciences). Data analysis was performed using FlowJo software (Tristar). Sorted populations were >95% pure. Cell suspensions were stained with anti-CD45 (30-F11), anti-TER119 (TER-119), TCRβ (H57-597), anti-CD3ε (eBio500A2), anti-CD19 (eBio1D3), anti-NK1.1 (PK136), anti-CD11c (N418), anti-Gr1 (RB6-8C5), anti-CD11b (Mi/70), anti-CCR6 (29-2L17), anti-CD127 (IL-7Rα; A7R34), anti-Thy1.2 (53-2.1), anti-CD49b (DX5), anti-TCRδ (GL3), anti-NKp46 (29A1.4), anti-IL-17 (eBio17B7), anti-IL-22 (1H8PWSR), rat IgG1 isotype control (eBRG1) antibodies, 7AAD viability dye, anti-mouse CD16/CD32 (Fc block), anti-RORγt (AFKJS-9); rat IgG2aₖ isotype control (eBR2a) and streptavidin fluorochrome conjugates all from eBioscience; anti-CD4 (GK1.5), anti-CD31 (390), anti-CD8α (53-6.7), anti-CD24 (M1/69), anti-Epcam (G8.8) antibodies were purchased from Biolegend. Anti-RET (IC718A) antibody was purchased from R&D Systems. LIVE/DEAD Fixable Aqua Dead Cell Stain Kit was purchased from Invitrogen. Cell populations were defined as: ILC3 - CD45⁺Lin⁻Thy1.2ʰⁱIL7Rα⁺RORγt⁺. For ILC3 subsets, additional markers were employed: LTi - CCR6⁺Nkp46⁻; ILC3 NCR⁻ - CCR6⁻Nkp46⁻; ILC3 NCR⁺ - CCR6⁻Nkp46⁺. Lineage was composed from CD3ε, CD8α, TCRβ, TCRγδ, CD19, Gr1, CD11c and TER119. Glial cells - CD45⁻CD31⁻TER119⁻CD49b⁺ (ref. 47); T cells - CD45⁺CD3ε⁺; γδ T cells - CD45⁺CD3ε⁺γδTCR⁺; B cells - CD45⁺CD19⁺B220⁺; macrophages - CD45⁺CD11b⁺F4/80⁺; dendritic cells - CD45⁺CD19⁻CD3ε⁻MHCII⁺CD11c⁺; enteric neurons - CD45⁻RET/GFP⁺ (ref. 13); epithelial cells - CD45⁻CD24⁺Epcam⁺.

**Quantitative RT–PCR.** Total RNA was extracted using RNeasy micro kit (Qiagen) or Trizol (Invitrogen) according to the manufacturer's protocol. RNA concentration was determined using Nanodrop Spectrophotometer (Nanodrop Technologies). Quantitative real-time reverse transcription (RT)–PCR was performed as previously described[2,8,9]. *Hprt* and *Gapdh* were used as housekeeping genes. For TaqMan assays (Applied Biosystems), RNA was retro-transcribed using a High Capacity RNA-to-cDNA Kit (Applied Biosystems), followed by a pre-amplification PCR using TaqMan PreAmp Master Mix (Applied Biosystems). TaqMan Gene Expression Master Mix (Applied Biosystems) was used in real-time PCR. TaqMan Gene Expression Assays (Applied Biosystems) were the following: *Gapdh* Mm99999915_g1; *Hprt* Mm00446968_m1; *Artn* Mm00507845_m1; *Nrtn* Mm03024002_m1; *Gdnf* Mm00599849_m1; *Gfra1 Mm00439086_m1*; *Gfra2 Mm00433584_m1*; *Gfra3 Mm00494589_m1*; *Ret* Mm00436304_m1; *Il22* Mm01226722_g1; *Il17a* Mm00439618_m1; *Il23r* Mm00519943_m1; *Rorgt* Mm01261022_m1; *Il7ra* Mm00434295_m1; *Ahr* Mm00478932_m1; *Stat3* Mm01219775_m1; *Cxcr6* Mm02620517_s1; *Nfkbiz* Mm_00600522_m1; *Reg3a* Mm01181787_m1; *Reg3b* Mm00440616_g1; *Reg3g* Mm00441127_m1;

*Defa1* Mm02524428_g1; *Defa29* Mm00655850_m1; *Defa5* Mm00651548_g1; *Defa21* Mm04206099_gH; *Muc1* Mm00449599_m1; *Muc3* Mm01207064_m1; *Muc13* Mm00495397_m1; *Gfap* Mm01253033_m1; *Ascl2* Mm01268891_g; *Tff3* Mm00495590_m1; *Relm-b* Mm00445845_m1; *Pla2g2a* Mm00448160_m1; *Pla2g5* Mm00448162_m1; *Wnt3* Mm00437336_m1; *Ctnnb1* Mm00483039_ m1; *Axin2* Mm00443610_m1; *Dll1b* Mm01279269_m1; *Il18* Mm00434225_m1; *Tnfa* Mm00443260_g1; *Lyz1* Mm00657323_m1; *Lrg5* Mm00438890_m1; *Tbx21* Mm00450960_m1; *Id2* Mm00711781_m1; *Runx1* Mm01213404_m1; *Notch1* Mm00435249_m1; *Notch2* Mm00803077_m1; *Gata3* Mm00484683_m1; *Bcl2* Mm00477631_m1; *Bcl2l1* Mm00437783_m1; *Arntl* Mm00500226_m1; *Glpr2* Mm01329475_m1; *Gja1* Mm01179639_s1; *Ednrb* Mm00432989; *S100b* Mm00485897_m1; *Sox10* Mm00569909_m1. Real-time PCR analysis was performed using ABI Prism 7900HT Sequence Detection System or StepOne Real-Time PCR system (Applied Biosystems).

**ILC3 activation and cell signalling.** Sorted intestinal ILC3 cells were starved for 3 hours in RPMI at 37 °C in order to ensure ILC3 viability. *Ret*$^{fl}$ or *Ret*$^\Delta$ were analysed directly *ex vivo*. To test ERK, AKT, p38-MAPK (Cell Signaling Technology) and STAT3 (BD Pharmigen) upon GFL stimulation wild-type ILC3 were activated with 500 ng ml$^{-1}$ (each GFL) and co-receptors (recombinant rat (rr) GFR-α1, recombinant mouse (rm) GFR-α2, rrGFR-α3 and rrGNDF from R&D Systems; recombinant human (rh) NRTN and rhARTN from PeproTech) for 10 and 30 min. When referring to the use of 'GFL', we have employed GDNF, NRTN, ARTN and their specific co-receptors in combination. For inhibition experiments cells were incubated 1 h at 37 °C before GFL stimulation, to test ERK, AKT, p38/ MAPK and STAT3 phosphorylation, or during overnight stimulation with GFLs, to determine *Il22* expression levels. Inhibitors were purchased from Sigma-Aldrich; p38 MAPK/ERK-AKT, LY294002 (LY); ERK, PD98059 (PD); AKT, AKT Inhibitor VIII (VIII); p38 MAPK, SB 202190 (SB); and pSTAT3, S3I-201 (S3I).

**Chromatin immunoprecipitation (ChIP) assay.** Enteric ILC3 from adult C57BL/6J mice were isolated by flow cytometry. Cells were starved for 3 h with RPMI supplemented with 1% HEPES, sodium pyruvate, glutamine, streptomycin and penicillin and 0.1% β-mercaptoethanol (Gibco) at 37 °C. Cells were stimulated with GFLs (500 ng ml$^{-1}$ each)[8], lysed, cross-linked and chromosomal DNA–protein complex sonicated to generate DNA fragments ranging from 100–300 base pairs. DNA–protein complexes were immuno-precipitated, using LowCell ChIP kit (Diagenode)[18], with 3 μg of rabbit polyclonal antibody against anti-pSTAT3 (Cell Signalling Technology), rabbit control IgG (Abcam) or H3K36me3 (07-030; Millipore). Immunoprecipitates were uncross-linked and analysed by quantitative PCR using primer pairs (5'–3') flanking putative sites on *Il22*. Vehicle (BSA)-stimulated ILC3s were used as controls. *Il22* primer sequences were previously described[48–50], briefly: (a) forward: 5'-TGCAATCAATCCCAGTATTTTG-3' and reverse: 5'-CTTGTGCAAGCATAAGTCTCAA-3'; (b) forward: 5'-GAAGTTGGTGG GAAAATGAGTCCGTGA-3' and reverse: 5'-GCCATGGCCTTTGCCGTAG TAGATTCTG-3'; (c) forward: 5'-ACGGGAGATCAAAGGCTGCTCT-3' and reverse: 5'-GCCAACAAGGTGCTTTTGC-3'; (d) forward: 5'-CTCACC GTGACGTTTTAGGG-3' and reverse: 5'-GTGAATGATATGACATCAGAC-3'; (e) forward 5'-CGACGAACATGCTCCCCTGATGTTTTT-3' and reverse: 5'-AAACTCATAGATTTCTGCAGGACAGCC-3'; (f) forward: 5'-AGCTG CATCTCTTTCTCTCCA-3' and reverse: 5'-TATCCTGAAGGCCAA AATAGGA-3'; (g) forward: 5'-ACGACCAGAACATCCAGAAGA-3' and reverse: 5'-GCAGAGAAAGAAATCCCCGC-3'; (h) forward: 5'-AGGGGGAC TTGCTTTGCCATTT-3' and reverse: 5'-AACACCCCTTCTTTCC TCCTCCAT-3'; (i) forward: 5'-CTGCTCCTTCCTGCCTTCTA-3' and reverse: 5'-CTGAGCCAGGTTTCATGTGA-3'. Primer positions are shown in Fig. 3i relative to the transcription start codon of *Il22*.

**Colony-forming units and paracellular permeability.** Organs were collected, weighed, and brought into suspension. Bacterial colony-forming units were determined per gram of tissue and total organ. Colony-forming units were determined by serial dilutions on Luria Broth (LB) agar and MacConkey agar (Sigma-Aldrich). Colonies were counted after 2 days of culture at 37 °C. To address intestinal paracellular permeability 16 mg per mouse of Dextran-Fitc (Sigma Aldrich) were administrated by gavage after overnight starvation. Plasma was analysed after 4 hours of Dextran-Fitc administration using a Microplate Reader TECAN Infinity F500.

**BrdU administration and Ki-67 labeling.** BrdU was administrated by intraperitoneal injection (1.25 mg per mouse). For flow cytometric analysis of epithelial cell proliferation anti-BrdU (Staining Kit for flow Cytometry, eBioscience) and anti-mouse Ki-67 antibody (BioLegend) were used.

**Quantitative PCR analysis of bacteria in stool at the phylum level.** DNA from faecal pellet samples was isolated with ZR Fecal DNA MicroPrep (Zymo Research). Quantification of bacteria was determined from standard curves

established by qPCR. qPCR were performed with Power SYBR Green PCR Master Mix (Applied Biosystems) and different primer sets using a StepOne Plus (Applied Biosystems) thermocycler. Samples were normalized to 16S rDNA and reported according to the 2$^{\Delta\Delta Ct}$ method. Primer sequences were: 16S rDNA, forward: 5'-ACTCCTACGGGAGGCAGCAGT-3' and reverse: 5'-ATTACCGCGGCTGCTGGC-3'; *Firmicutes*, forward: 5'-ACTCCT ACGGGAGGCAGC-3' and reverse: 5'-GCTTCTTAGTCAGGTACCGTCAT-3'; *Bacteroidetes*, forward: 5'-GGTTCTGAGAGGAGGTCCC-3' and reverse: 5'-GCTGGCTCCCGTAGGAGT-3'; *Proteobacteria*, forward: 5'-GGTTC TGAGAGGAGGTCCC-3' and reverse 5'-GCTGGCTCCCGTAGGAGT-3'.

**16S rRNA quantification and gene sequencing.** Faeces were isolated from co-housed *Ret*$^{fl}$ or *Ret*$^\Delta$ littermates. Sequencing of the 16S *rRNA* gene was performed as previously described[51]. Briefly, barcoded primers were used to amplify the V4 region of the 16S rRNA gene, and the amplicons were sequenced on a MiSeq instrument (Illumina, San Diego, USA) using 150 bp, paired-end chemistry at the University of Pennsylvania Next Generation Sequencing Core. The paired ends were assembled and quality filtered, selecting for reads with a quality score ≥30. Reads with >10 bp homopolymers and reads shorter than 248 bp or longer than 255 bp were removed from the analysis. 16S rRNA sequence data were processed using mothur version 1.25.0 (ref. 52) and QIIME version 1.8 (ref. 53). Chimaeric sequences were removed with ChimeraSlayer[54]. Operational taxonomic units (OTUs) were defined with CD-HIT[55] using 97% sequence similarity as a cut-off. Only OTUs containing ≥2 sequences were retained; OTUs assigned to cyanobacteria or those which were not assigned to any phylum were removed from the analysis. Taxonomy was assigned using the Ribosomal Database Project (RDP) classifier v 2.2 (ref. 56), multiple sequence assignment was performed with PyNAST (v 1.2.2)[57], and FastTree[58] was used to build the phylogeny. Samples were rarified to 22,000 sequences per sample for alpha- and beta-diversity analyses. Taxonomic relative abundances are reported as the median with standard deviation. *P* values were calculated using the Wilcoxon rank-sum test. Statistical tests were conducted in R version 3.2.0. To determine which factors were associated with microbial community composition, statistical tests were performed using the non-parametric analysis of similarities (ANOSIM) with weighted UniFrac distance metrics[59].

**Data accession.** The sequencing data generated in this study have been submitted to the NCBI Sequence Read Archive under BioProject PRJNA314493 (SRA: http://www.ncbi.nlm.nih.gov/sra/?term=PRJNA314493).

**Intestinal organoids.** IntestiCult Organoid Growth Medium and Gentle Cell Dissociation Reagent were purchased from StemCell. Intestinal crypts were isolated from C57BL/6J mice according to the manufacturer's instructions and were added to previously thawed, ice-cold Matrigel at a 1:1 ratio and at a final concentration of 5,000–7,000 crypts per ml. 15 μl of this mix was plated per well of a 96-well round-bottom plate. After Matrigel solidification 100 μl of growth medium (100 U ml$^{-1}$ penicillin/streptomycin) was added and replaced every 3 days. Organoids were grown at 37 °C with 5% CO$_2$ and passaged according to the manufacturer's instructions. Freshly sorted intestinal ILC3 were added to 5–8 days old epithelial organoids after plating for 24 hours with or without anti-mouse IL-22 antibody (R&D Systems).

**IL-22 agonist administration *in vivo*.** 150 μg of anti-IL-22 antibody (8E11; gift from Genentech) or mouse IgG1 isotype control (MOPC-21; Bio X Cell) was administered by intraperitoneal injection to *Ret*$^{MEN2B}$ mice every 2 days. Animals were analysed 2 weeks after the first administration.

**Neurosphere-derived glial cells.** Neurosphere-derived glial cells were obtained as previously described[60]. Briefly, total intestines from E14.5 C57BL/6J and *Myd88*$^{-/-}$ mice were digested with collagenase D (0.5 mg ml$^{-1}$; Roche) and DNase I (0.1 mg ml$^{-1}$; Roche) in DMEM/F-12, GlutaMAX, supplemented with 1% HEPES, streptomycin/penicillin and 0.1% β-mercaptoethanol (Gibco) for approximately 30 min at 37 °C under gentle agitation. Cells were cultured for 1 week in a CO$_2$ incubator at 37 °C in DMEM/F-12, GlutaMAX, streptomycin and penicillin and 0.1% β-mercaptoethanol (Gibco) supplemented with B27 (Gibco), EGF (Gibco) and FGF2 (Gibco) 20 ng ml$^{-1}$. After 1 week of culture cells were treated with 0.05% trypsin (Gibco), transferred into PDL (Sigma-Aldrich) coated plates and culture in DMEM supplemented with 10% FBS, 1% HEPES, glutamine, streptomycin and penicillin and 0.1% β-mercaptoethanol (Gibco) until confluence. Glial cells were activated with TLR2 (5 μg ml$^{-1}$) (Pam3CSK4), TLR3 (100 μg ml$^{-1}$) (PolyI:C), TLR4 (50 μg ml$^{-1}$) (LPS), TLR9 (50 μg ml$^{-1}$) (DsDNA-EC) ligands from Invivogen and IL-1β (10 μg ml$^{-1}$) (401ML005), IL-18 (50 μg ml$^{-1}$) (B002-5), IL-33 (0.1 μg ml$^{-1}$) (3626ML) recombinant proteins from R&D Systems. Cells were also co-cultured with purified ILC3 from wild-type and *Il1b*-deficient mice. IL-22 expression in glial-ILC3 co-cultures upon TLR4 activation was also performed using GDNF (2 μg ml$^{-1}$) (AB-212–NA), NRTN (2 μg ml$^{-1}$) (AF-387sp) and ARTN (0.3 μg ml$^{-1}$) (AF-1085-sp) blocking antibodies. Cells were analysed after 24 hours of co-culture.

**Statistics.** Results are shown as mean ± s.e.m. Statistical analysis used Microsoft Excel. Variance was analysed using $F$-test. Student's $t$-test was performed on homoscedastic populations, and Student's $t$-test with Welch correction was applied on samples with different variances. Analysis of survival curves was performed using a MAntel–Cox test. Results were considered significant at $*P \leq 0.05$ and $**P \leq 0.01$. Statistical treatment of metagenomics analysis is described in the Methods section '16S rRNA gene sequencing and analysis'.

31. Cao, X. et al. Defective lymphoid development in mice lacking expression of the common cytokine receptor γ chain. Immunity **2,** 223–238 (1995).
32. Mombaerts, P. et al. RAG-1-deficient mice have no mature B and T lymphocytes. Cell **68,** 869–877 (1992).
33. Srinivas, S. et al. Cre reporter strains produced by targeted insertion of EYFP and ECFP into the ROSA26 locus. BMC Dev. Biol. **1,** 4 (2001).
34. Madisen, L. et al. A robust and high-throughput Cre reporting and characterization system for the whole mouse brain. Nat. Neurosci. **13,** 133–140 (2010).
35. Horai, R. et al. Production of mice deficient in genes for interleukin (IL)-1α, IL-1β, IL-1α/β, and IL-1 receptor antagonist shows that IL-1β is crucial in turpentine-induced fever development and glucocorticoid secretion. J. Exp. Med. **187,** 1463–1475 (1998).
36. Adachi, O. et al. Targeted disruption of the MyD88 gene results in loss of IL-1- and IL-18-mediated function. Immunity **9,** 143–150 (1998).
37. Wiles, S., Pickard, K. M., Peng, K., MacDonald, T. T. & Frankel, G. In vivo bioluminescence imaging of the murine pathogen Citrobacter rodentium. Infect. Immun. **74,** 5391–5396 (2006).
38. Collins, J. W. et al. Citrobacter rodentium: infection, inflammation and the microbiota. Nat. Rev. Microbiol. **12,** 612–623 (2014).
39. Ibiza, S. et al. Endothelial nitric oxide synthase regulates T cell receptor signaling at the immunological synapse. Immunity **24,** 753–765 (2006).
40. Moolenbeek, C. & Ruitenberg, E. J. The "Swiss roll": a simple technique for histological studies of the rodent intestine. Lab. Anim. **15,** 57–59 (1981).
41. Burich, A. et al. Helicobacter-induced inflammatory bowel disease in IL-10- and T cell-deficient mice. Am. J. Physiol. Gastrointest. Liver Physiol. **281,** G764–G778 (2001).
42. Fort, M. M. et al. A synthetic TLR4 antagonist has anti-inflammatory effects in two murine models of inflammatory bowel disease. J. Immunol. **174,** 6416–6423 (2005).
43. Seamons, A., Treuting, P. M., Brabb, T. & Maggio-Price, L. Characterization of dextran sodium sulfate-induced inflammation and colonic tumorigenesis in Smad3−/− mice with dysregulated TGFβ. PLoS One **8,** e79182 (2013).
44. Bogunovic, M. et al. Origin of the lamina propria dendritic cell network. Immunity **31,** 513–525 (2009).
45. Muller, P. A. et al. Crosstalk between muscularis macrophages and enteric neurons regulates gastrointestinal motility. Cell **158,** 300–313 (2014).
46. Sanos, S. L. & Diefenbach, A. Isolation of NK cells and NK-like cells from the intestinal lamina propria. Methods Mol. Biol. **612,** 505–517 (2010).
47. Joseph, N. M. et al. Enteric glia are multipotent in culture but primarily form glia in the adult rodent gut. J. Clin. Invest. **121,** 3398–3411 (2011).
48. Escobar, T. M. et al. miR-155 activates cytokine gene expression in Th17 cells by regulating the DNA-binding protein Jarid2 to relieve polycomb-mediated repression. Immunity **40,** 865–879 (2014).
49. Guo, X. et al. Induction of innate lymphoid cell-derived interleukin-22 by the transcription factor STAT3 mediates protection against intestinal infection. Immunity **40,** 25–39 (2014).
50. Yeste, A. et al. IL-21 induces IL-22 production in CD4+ T cells. Nat. Commun. **5,** 3753 (2014).
51. Misic, A. M. et al. The shared microbiota of humans and companion animals as evaluated from Staphylococcus carriage sites. Microbiome **3,** 2 (2015).
52. Schloss, P. D. et al. Introducing mothur: open-source, platform-independent, community-supported software for describing and comparing microbial communities. Appl. Environ. Microbiol. **75,** 7537–7541 (2009).
53. Caporaso, J. G. et al. QIIME allows analysis of high-throughput community sequencing data. Nat. Methods **7,** 335–336 (2010).
54. Haas, B. J. et al. Chimeric 16S rRNA sequence formation and detection in Sanger and 454-pyrosequenced PCR amplicons. Genome Res. **21,** 494–504 (2011).
55. Fu, L., Niu, B., Zhu, Z., Wu, S. & Li, W. CD-HIT: accelerated for clustering the next-generation sequencing data. Bioinformatics **28,** 3150–3152 (2012).
56. Wang, Q., Garrity, G. M., Tiedje, J. M. & Cole, J. R. Naive Bayesian classifier for rapid assignment of rRNA sequences into the new bacterial taxonomy. Appl. Environ. Microbiol. **73,** 5261–5267 (2007).
57. Caporaso, J. G. et al. PyNAST: a flexible tool for aligning sequences to a template alignment. Bioinformatics **26,** 266–267 (2010).
58. Price, M. N., Dehal, P. S. & Arkin, A. P. FastTree: computing large minimum evolution trees with profiles instead of a distance matrix. Mol. Biol. Evol. **26,** 1641–1650 (2009).
59. Lozupone, C., Hamady, M. & Knight, R. UniFrac—an online tool for comparing microbial community diversity in a phylogenetic context. BMC Bioinformatics **7,** 371 (2006).
60. Mich, J. K. et al. Prospective identification of functionally distinct stem cells and neurosphere-initiating cells in adult mouse forebrain. eLife **3,** e02669 (2014).
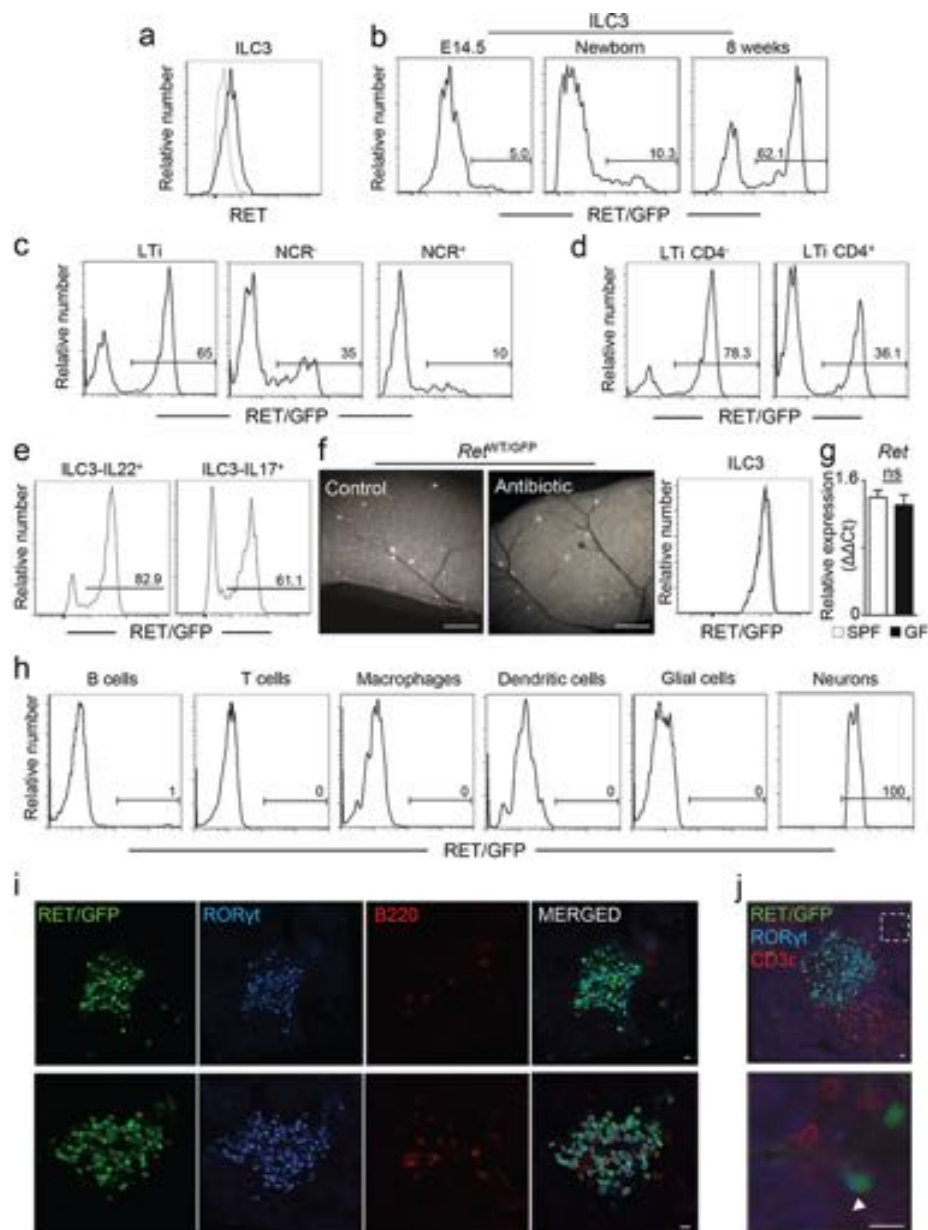
**Extended Data Figure 1 | ILC3 selectively express the neurotrophic factor receptor RET. a**, Expression of RET protein in gut CD45$^+$Lin$^-$Thy1.2$^{hi}$IL7R$\alpha^+$ROR$\gamma$t$^+$ ILC3. **b**, Analysis of gut ILC3 from $Ret^{GFP}$ mice. Embryonic day 14.5 (E14.5). **c, d**, Analysis of enteric ILC3 subsets from $Ret^{GFP}$ mice. **e**, Analysis of cytokine-producing ILC3 from $Ret^{GFP}$ mice. **f**, Pregnant $Ret^{GFP}$ mice were provided with antibiotic cocktails that were maintained after birth until analysis at 6 weeks of age. Left, RET/GFP (white); right, flow cytometry analysis of RET/GFP expression in ILC3. Thin line, Ab-treated; bold line, specific pathogen free (SPF). **g**, $Ret$ expression in enteric ILC3 from germ-free (GF) mice and SPF controls ($n = 4$). **h**, Analysis of lamina propria populations from $Ret^{GFP}$ mice. **i**, Enteric ILC3 clusters. Green, RET/GFP; blue, ROR$\gamma$t; red, B220. Bottom, quantification analysis for RET/GFP and ROR$\gamma$t co-expression (79.97 $\pm$ 4.72%). **j**, Rare RET-expressing ILC3 in intestinal villi. Green, RET/GFP; blue, ROR$\gamma$t; red, CD3$\varepsilon$. Scale bars, 10$\mu$m. Data are representative of 4 independent experiments. Error bars show s.e.m.
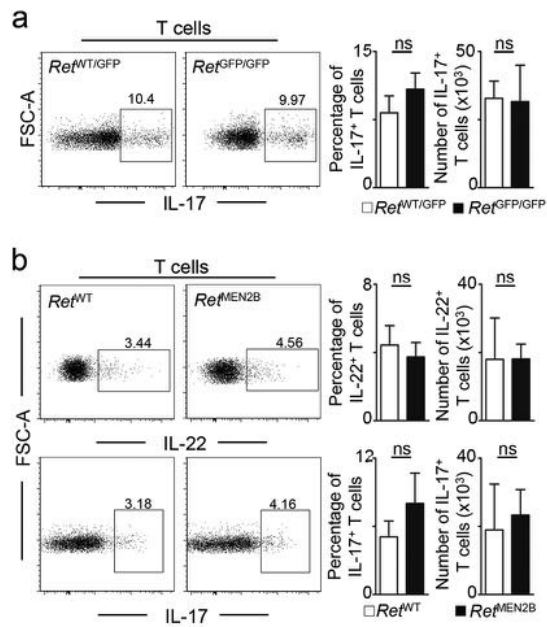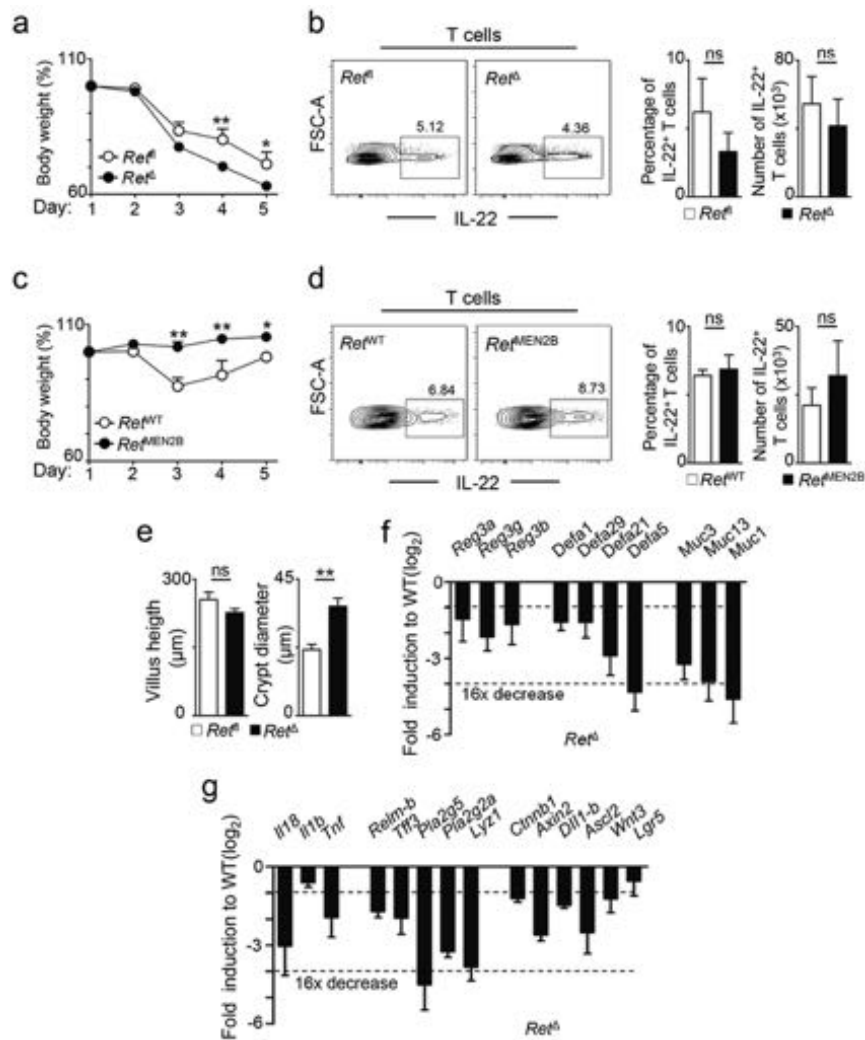
**Extended Data Figure 2 | T cell-derived IL-22 and IL-17 in $Ret^{GFP}$ chimaeras and $Ret^{MEN2B}$ mice. a**, T-cell-derived IL-17 in $Ret^{GFP}$ chimaeras. $Ret^{WT/GFP}$, $n = 25$; $Ret^{GFP/GFP}$, $n = 22$. **b**, T-cell-derived IL-22 and IL-17 in the intestine of $Ret^{MEN2B}$ mice and their wild-type littermate controls ($n = 7$). Data are representative of 4 independent experiments. Error bars show s.e.m.
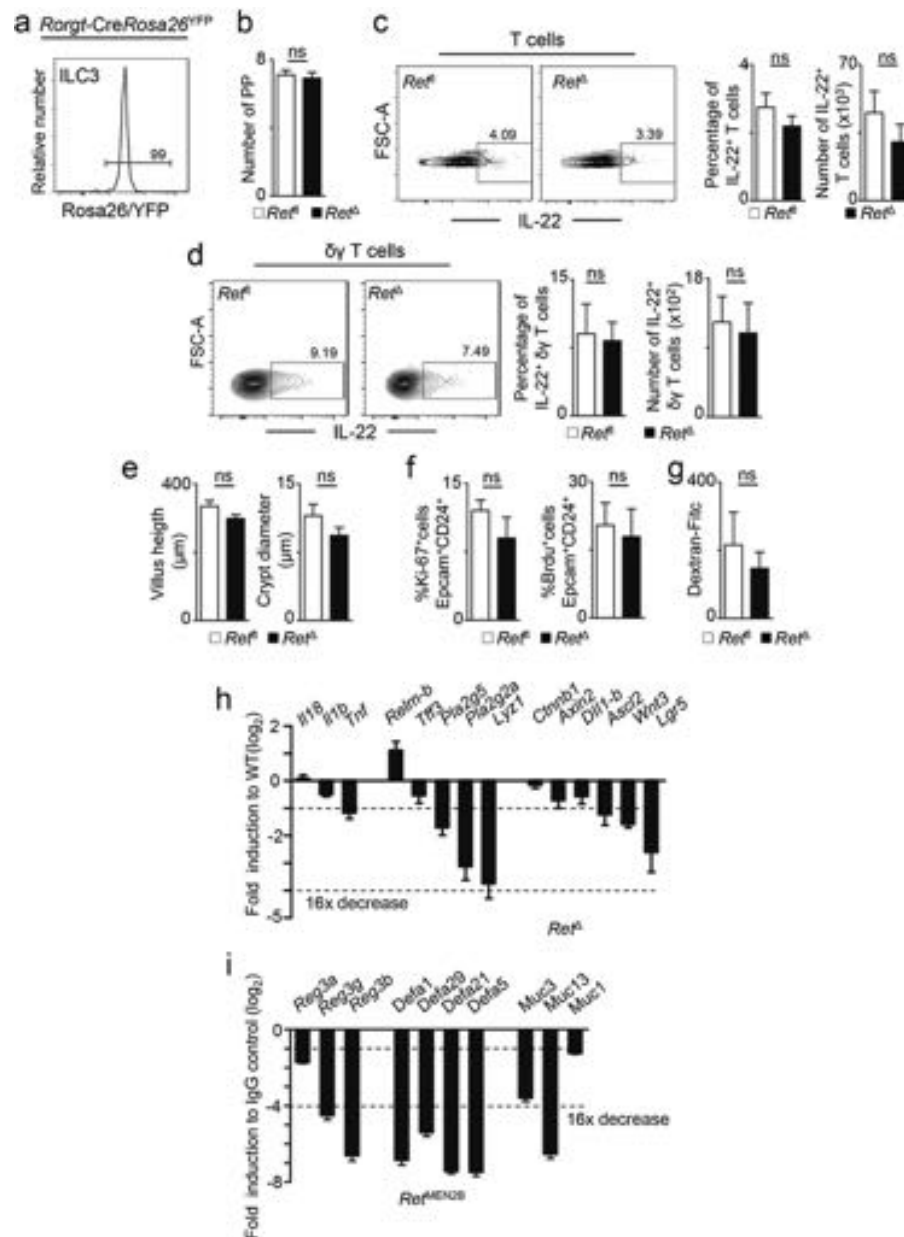
**Extended Data Figure 3 | Enteric homeostasis in steady-state $Ret^\Delta$ mice.** **a**, *Rorgt*-Cre mice were bread to *Rosa26*[YFP] mice. Analysis of Rosa26/YFP expression in gut ILC3 from *Rorgt*-Cre*Rosa26*[YFP] mice. **b**, Number of Peyer's patches (PP) ($n=10$). **c**, T-cell-derived IL-22 in $Ret^\Delta$ mice and their wild-type littermate controls. ($n=11$). **d**, $\gamma\delta$ T-cell-derived IL-22 in $Ret^\Delta$ mice and their wild-type littermate controls ($n=4$). **e**, Intestinal villus and crypt morphology ($n=6$). **f**, Epithelial cell proliferation ($n=5$). **g**, Intestinal paracellular permeability measured by Dextran-Fitc in the plasma ($n=5$). **h**, Tissue repair genes in $Ret^\Delta$ intestinal epithelium in comparison to their wild-type littermate controls ($n=8$). **i**, Reactivity genes in $Ret^{MEN2B}$ mice treated with anti-IL-22 blocking antibodies compared to $Ret^{MEN2B}$ intestinal epithelium. $Ret^{MEN2B}$, $n=4$; $Ret^{MEN2B}$ + anti-IL-22, $n=4$. Data are representative of 3 independent experiments. Error bars show s.e.m.

**Extended Data Figure 4 | Enteric inflammation in mice with altered RET signals.** Mice were treated with DSS in the drinking water. **a**, Weight loss of DSS-treated $Ret^\Delta$ mice and their littermate controls ($n = 8$). **b**, T-cell-derived IL-22 in $Ret^\Delta$ mice and their wild-type littermate controls after DSS treatment ($n = 8$). **c**, Weight loss of DSS treated $Ret^{MEN2B}$ mice and their wild-type littermate controls ($n = 8$). **d**, T-cell-derived IL-22 in $Ret^{MEN2B}$ mice and their wild-type littermate controls ($n = 8$). **e**, Intestinal villi and crypt morphology ($n = 6$). **f**, Epithelial reactivity gene expression in DSS treated $Ret^\Delta$ mice in comparison to their wild-type littermate controls ($n = 8$). **g**, Tissue repair gene expression in DSS treated $Ret^\Delta$ mice in comparison to their wild-type littermate controls ($n = 4$). Data are representative of 3–4 independent experiments. Error bars show s.e.m. *$P < 0.05$; **$P < 0.01$.
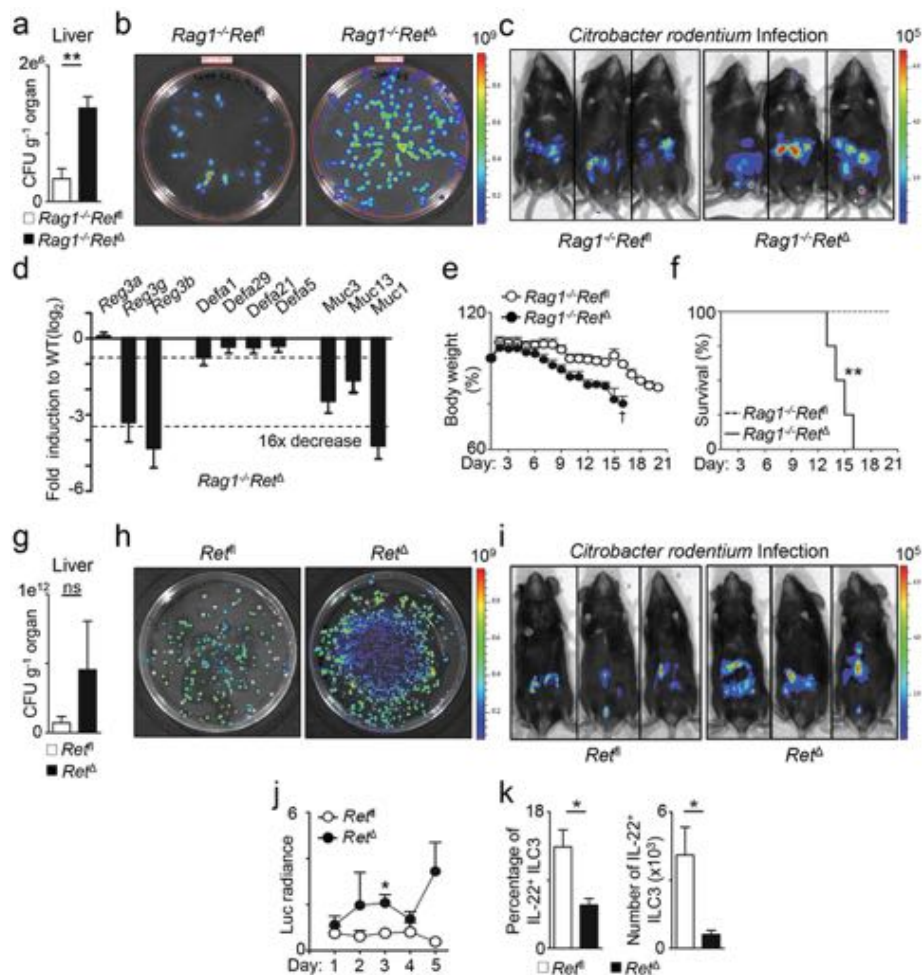
**Extended Data Figure 5 | *Citrobacter rodentium* infection in *Ret*$^\Delta$ mice. a**, *C. rodentium* translocation to the liver of *Rag1*$^{-/-}$*Ret*$^\Delta$ and their *Rag1*$^{-/-}$*Ret*$^{fl}$ littermate controls at day 6 after infection (*n* = 15). **b**, MacConkey plates of liver cell suspensions from *Rag1*$^{-/-}$*Ret*$^\Delta$ and their *Rag1*$^{-/-}$*Ret*$^{fl}$ littermate controls at day 6 after *C. rodentium* infection. **c**, Whole-body imaging of *Rag1*$^{-/-}$*Ret*$^\Delta$ and their *Rag1*$^{-/-}$*Ret*$^{fl}$ littermate controls at day 6 after luciferase-expressing *C. rodentium* infection. **d**, Epithelial reactivity gene expression in *C. rodentium* infected *Rag1*$^{-/-}$*Ret*$^\Delta$ mice (n = 17) and their *Rag1*$^{-/-}$*Ret*$^{fl}$ littermate controls (*n* = 15). **e**, Weight loss in *C. rodentium*-infected *Rag1*$^{-/-}$*Ret*$^\Delta$ mice and their *Rag1*$^{-/-}$*Ret*$^{fl}$ littermate controls (*n* = 8). **f**, Survival curves in

*C. rodentium* infected *Rag1*$^{-/-}$*Ret*$^\Delta$ mice and their *Rag1*$^{-/-}$*Ret*$^{fl}$ littermate controls (*n* = 8). **g**, *C. rodentium* translocation to the liver of *Ret*$^\Delta$ and their *Ret*$^{fl}$ littermate controls at day 6 after infection (*n* = 6). **h**, MacConkey plates of liver cell suspensions from *Ret*$^\Delta$ and their *Ret*$^{fl}$ littermate controls at day 6 after *C. rodentium* infection. **i**, Whole-body imaging of *Ret*$^\Delta$ and their *Ret*$^{fl}$ littermate controls at day 6 after luciferase-expressing *C. rodentium* infection. **j**, *C. rodentium* infection burden (*n* = 8). **k**, Innate IL-22 in in *C. rodentium* infected *Ret*$^\Delta$ mice and their *Ret*$^{fl}$ littermate controls (*n* = 8). Data are representative of 3–4 independent experiments. Error bars show s.e.m. ns, not significant. *$P < 0.05$; **$P < 0.01$.
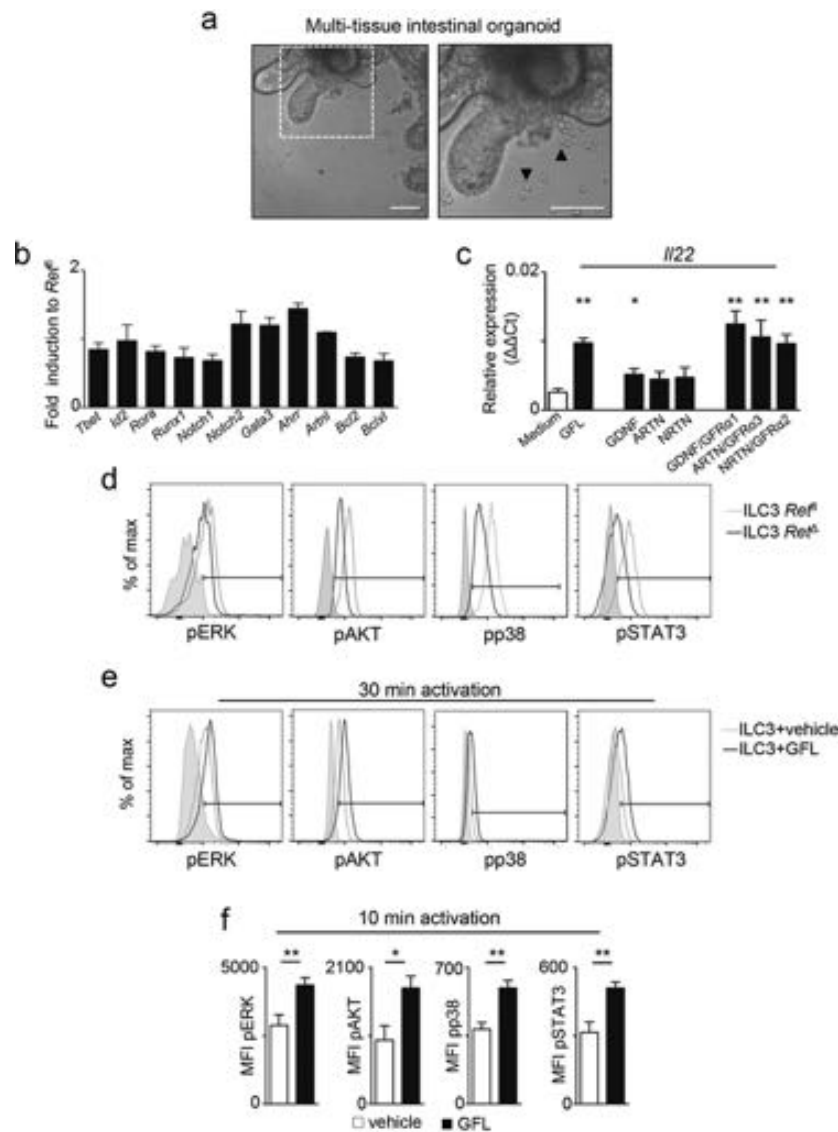
**Extended Data Figure 6 | Glial-derived neurotrophic factor family ligand (GFL) signals in ILC3. a**, Multi-tissue intestinal organoid system. Scale bar, 20μm. Black arrows, ILC3. **b**, Expression of ILC-related genes in ILC3 from $Ret^\Delta$ mice in comparison to their littermate controls ($n = 4$). **c**, ILC3 activation with all GFL/GFRα pairs (GFL); single GDNF family ligand (GDNF, ARTN or NRTN); or single GFL/GFRα pairs (GDNF/ GFRα1, ARTN/GFRα3 or NRTN/GFRα2) compared to vehicle BSA ($n = 5$). **d**, ILC3 from $Ret^\Delta$ mice (open black) and their littermate controls (open dash). Isotype (closed grey). **e**, 30-min activation of ILC3 by GFL (open black) compared to vehicle BSA (open dash). Isotype (closed grey). **f**, 10-min activation of ILC3 by GFL. pERK, $n = 8$; pAKT, $n = 8$; phosphorylated p38/MAP kinase, $n = 8$; pSTAT3, $n = 8$. Similar results were obtained in at least 3–4 independent experiments. Error bars show s.e.m. *$P < 0.05$; **$P < 0.01$.
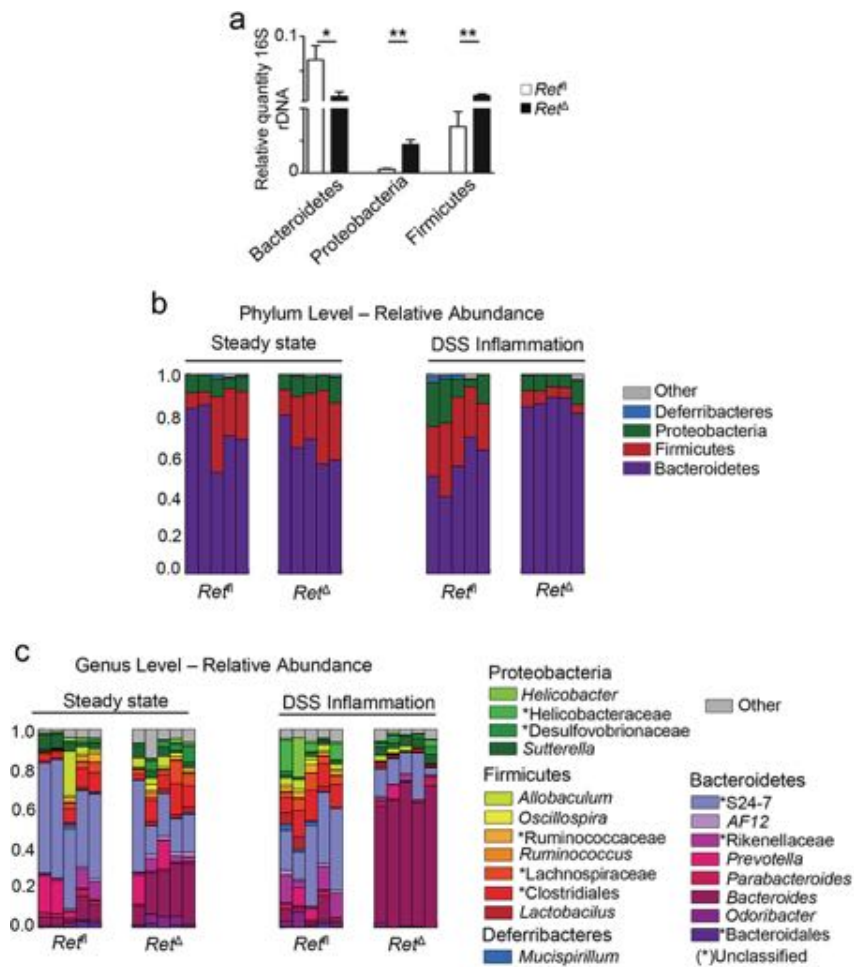
**Extended Data Figure 7 | Alterations in the diversity of intestinal commensal bacteria of $Ret^{\Delta}$ mice. a**, Quantitative PCR analysis at the phylum level in stool from co-housed $Ret^{fl}$ and $Ret^{\Delta}$ littermates in steady state ($n = 5$). **b**, Metagenomic phylum level comparisons in stool bacterial from co-housed $Ret^{fl}$ and $Ret^{\Delta}$ littermates in steady state (left) and after DSS treatment (right) ($n = 5$). **c**, Genus-level comparisons in stool bacteria from co-housed $Ret^{fl}$ and $Ret^{\Delta}$ littermates in steady state (left) and after DSS treatment (right) ($n = 5$). Error bars show s.e.m. *$P < 0.05$; **$P < 0.01$.
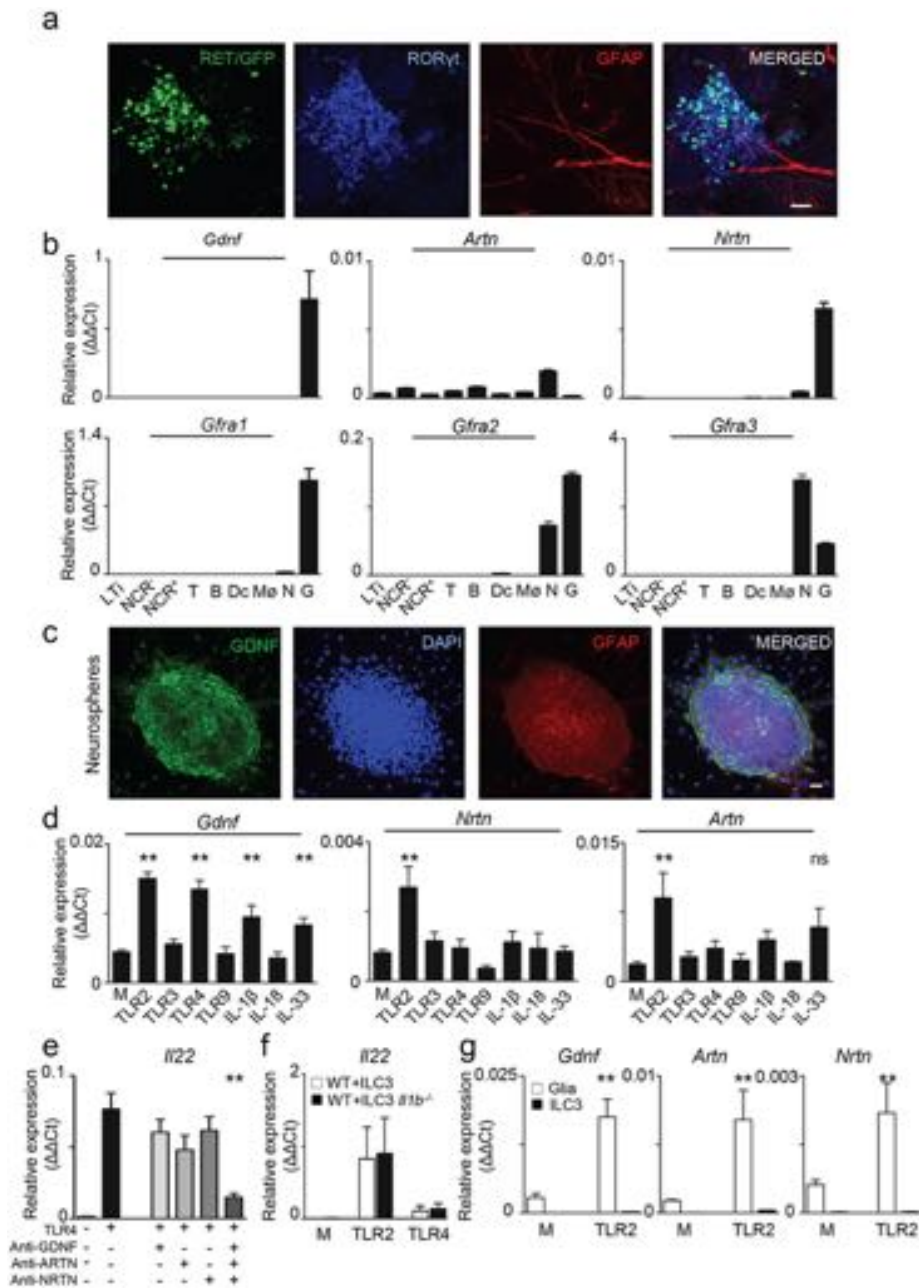
**Extended Data Figure 8 | GFL-expressing glial cells anatomically co-localize with ILC3. a,** Intestine of $Ret^{GFP}$ mice. Green, RET/GFP; red, GFAP; blue, RORγt. Similar results were obtained in 3 independent experiments. **b,** Purified lamina propria LTi, NCR⁻ and NCR⁺ ILC3 subsets, T cells (T), B cells (B), dendritic cells (Dc), macrophages (Mø), enteric neurons (N) and mucosal glial cells (G). **c,** Neurosphere-derived glial cells. **d,** Activation of neurosphere-derived glial cells with TLR2

(Pam3CSK4), TLR3 (Poli I:C), TLR4 (LPS) and TLR9 (DsDNA-EC) ligands, as well as IL-1β, IL-18 and IL-33 ($n = 6$). M, medium. **e,** $Il22$ in co-cultures of glial and ILC3 using single or combined GFL antagonists ($n = 6$). **f,** $Il22$ in co-cultures of ILC3 and glial cells from $Il1b^{-/-}$ or their wild-type controls ($n = 3$). **g,** $Gdnf$, $Artn$ and $Nrtn$ expression in glial cells and ILC3 upon TLR2 stimulation ($n = 3$). Scale bar, 30 μm. Similar results were obtained in at least 4 independent experiments.
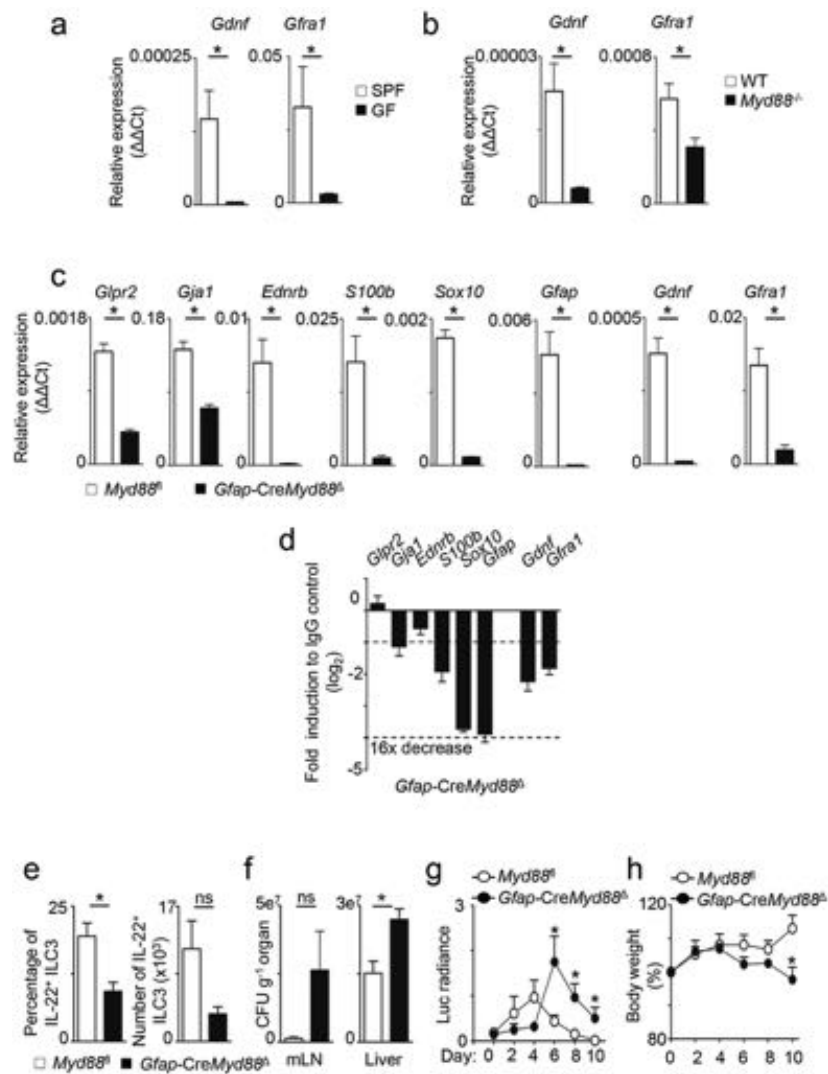
**Extended Data Figure 9 | Glial cell sensing via MYD88 signals.**
**a–c**, Intestinal glial cells were purified by flow cytometry. **a**, Germ-free and their respective SPF controls ($n = 3$). **b**, Myd88$^{-/-}$ and their respective wild-type littermate controls ($n = 3$). **c**, *Gfap*-Cre*Myd88*$^{\Delta}$ and their littermate controls (*Myd88*$^{fl}$) ($n = 3$). **d**, Total lamina propria cells of *Gfap*-Cre*Myd88*$^{\Delta}$ and their littermate controls (*Myd88*$^{fl}$) ($n = 6$).

**e–h**, *Citrobacter rodentium* infection of *Gfap*-Cre*Myd88*$^{\Delta}$ mice and their littermate controls (*Myd88*$^{fl}$) ($n = 6$). **e**, Innate IL-22. **f**, *Citrobacter rodentium* translocation. **g**, Infection burden. **h**, Weight loss. Data are representative of 3 independent experiments. Error bars show s.e.m. $*P < 0.05$; $**P < 0.01$.
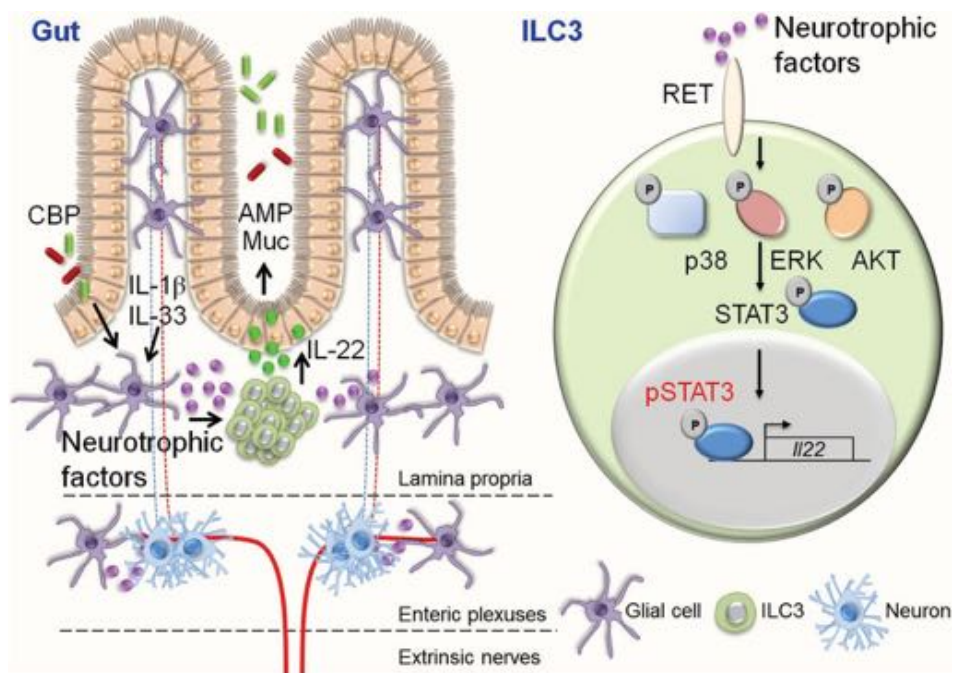
**Extended Data Figure 10 | A novel glial-ILC3-epithelial cell unit orchestrated by neurotrophic factors.** Lamina propria glial cells sense microenvironmental products that control neurotrophic factor expression. Glial-derived neurotrophic factors operate in an ILC3-intrinsic manner by activating the tyrosine kinase RET, which directly regulates innate IL-22 downstream of a p38 MAPK/ERK-AKT cascade and STAT3 phosphorylation. GFL induced innate IL-22 acts on epithelial cells to induce reactivity gene expression (CBP, commensal bacterial products; AMP, antimicrobial peptides; Muc, mucins). Thus, neurotrophic factors are the molecular link between glial cell sensing, innate IL-22 production and intestinal epithelial barrier defence.